

Instabilities and transient growth of the stratified Taylor–Couette flow in a Rayleigh-unstable regime

Junho Park^{1,†}, Paul Billant² and Jong-Jin Baik¹

¹School of Earth and Environmental Sciences, Seoul National University,
Seoul 151-742, Republic of Korea

²LadHyX, CNRS, Ecole Polytechnique, F-91128 Palaiseau CEDEX, France

(Received 27 August 2016; revised 1 April 2017; accepted 14 April 2017)

The stability of the Taylor–Couette flow is analysed when there is a stable density stratification along the axial direction and when the flow is centrifugally unstable, i.e. in the Rayleigh-unstable regime. It is shown that not only the centrifugal instability but also the strato-rotational instability can occur. These two instabilities can be explained and well described by means of a Wentzel–Kramers–Brillouin–Jeffreys asymptotic analysis for large axial wavenumbers in inviscid and non-diffusive limits. In the presence of viscosity and diffusion, numerical results reveal that the strato-rotational instability becomes dominant over the centrifugal instability at the onset of instability when the axial density stratification is sufficiently strong. Linear transient energy growth is next investigated for counter-rotating cylinders in the stable regime of the Froude number–Reynolds number parameter space. We show that there exist two types of transient growth mechanism analogous to the lift up and the Orr mechanisms in homogeneous fluids but with the additional effect of density perturbations. The dominant mechanism depends on the stratification: when the stratification is strong, non-axisymmetric three-dimensional perturbations achieve the optimal energy growth through the Orr mechanism while for moderate stratification, axisymmetric perturbations lead to the optimal transient growth by a lift-up mechanism involving internal waves.

Key words: instability, stratified flows, Taylor–Couette flow

1. Introduction

The Taylor–Couette flow, a flow between two independently rotating concentric cylinders, has been investigated for decades (Taylor 1923; Coles 1965; Andereck, Liu & Swinney 1986), and is still popular and being actively investigated nowadays (see e.g. Grossmann, Lohse & Sun 2016) to understand typical characteristics of fluid flows such as stability, transition, intermittency, bifurcation, turbulence, etc. In particular, the stability of the Taylor–Couette flow has received much attention in

† Email address for correspondence: jhsise@gmail.com

the fluid mechanics community. The angular velocity of the steady and axisymmetric base flow is

$$\Omega(r) = A + \frac{B}{r^2}, \quad A = \frac{r_o^2 \Omega_o - r_i^2 \Omega_i}{r_o^2 - r_i^2}, \quad B = \frac{r_i^2 r_o^2 (\Omega_i - \Omega_o)}{r_o^2 - r_i^2}, \quad (1.1a-c)$$

where r_i , r_o and Ω_i , Ω_o are the radius and the angular velocity of the inner and outer cylinders, respectively. According to the Rayleigh criterion (Rayleigh 1917), inviscid rotating flows are centrifugally unstable if there is a radius r where the Rayleigh discriminant $\phi(r) = (1/r^3) \partial(r^4 \Omega^2) / \partial r$ is negative, i.e. if the circulation decreases with r . The centrifugal instability (CI) tends to restore a non-decreasing circulation by secondary motions. According to the Rayleigh criterion, the flow (1.1) is centrifugally unstable if $\mu < \eta^2$ where $\mu = \Omega_o / \Omega_i$ and $\eta = r_i / r_o$. In this paper, we refer to this regime $\mu < \eta^2$ as the Rayleigh-unstable regime, i.e. inviscidly unstable (Maretzke, Hof & Avila 2014). While Rayleigh (1917) considered only axisymmetric perturbations to derive this criterion, a generalized criterion for non-axisymmetric perturbations has been obtained recently by means of the Wentzel–Kramers–Brillouin–Jeffreys (WKBJ) approximation (Billant & Gallaire 2005, 2013).

The Taylor–Couette flow with a stable axial stratification has also received much attention from geophysicists and astrophysicists since it serves as a model for equatorial flows in the atmosphere and oceans (Hitchman *et al.* 1987; Hua, Moore & Le Gentil 1997*b*), or as a model for the Keplerian flow in accretion disks (Dubrulle *et al.* 2005*a,b*). Withjack & Chen (1974, 1975), Boubnov, Gledzer & Hopfinger (1995) and Caton, Janiaud & Hopfinger (2000) have mainly considered the regime where only the inner cylinder rotates ($\mu = 0 < \eta^2$) which is centrifugally unstable. They have shown both numerically and experimentally that the stratification tends to suppress the CI. More recent work for arbitrary rotations of the two cylinders has revealed that there exists another type of instability, called the strato-rotational instability (SRI), which is due to a resonant interaction between inertia–gravity waves trapped near the inner and outer cylinders (Molemaker, McWilliams & Yavneh 2001; Yavneh, McWilliams & Molemaker 2001; Dubrulle *et al.* 2005*b*; Shalybkov & Rüdiger 2005; Le Bars & Le Gal 2007; Le Dizès & Riedinger 2010). These studies have shown that the stratified Taylor–Couette flow is inviscidly unstable in the range $\mu < 1$, which is wider than the Rayleigh-unstable regime $\mu < \eta^2$. Recently, Park & Billant (2013*b*) have shown that the SRI is also unstable when $\mu > 1$ so that the stratified Taylor–Couette flow is actually stable only for solid-body rotation ($\mu = 1$). They have also shown by means of a WKBJ analysis that the SRI is due to a reversal of the radial group velocity of the two boundary trapped waves at the critical point where the angular phase velocity of the waves equals the angular velocity of the base flow. Alternatively, this instability mechanism can be interpreted in terms of wave over-reflection at the critical point. The SRI has been mostly studied in the regime $\mu > \eta^2$ which is Rayleigh stable. Very recently, Leclercq, Nguyen & Kerswell (2016) have investigated the Rayleigh-unstable regime $\mu < \eta^2$. They have shown that the SRI and CI co-exist in this regime and they have studied their competition. Recent studies on vortices have also revealed that the CI is not always the dominant instability in the Rayleigh-unstable regime (Park 2012; Park & Billant 2013*a*).

In the present paper, we shall further study the competition between the SRI and CI in the regime $\mu < \eta^2$ in the inviscid limit and, then we shall map the dominant instability in the Froude number–Reynolds number parameter space. In contrast to Leclercq *et al.* (2016) who report that the SRI and CI are indistinguishable at onset,

the analyses of these two instabilities in the inviscid limit will enable us to track them as the Reynolds number is decreased and therefore distinguish the SRI from the CI at onset. In addition, much stronger stratification (up to six times) and higher azimuthal wavenumbers than considered by Leclercq *et al.* (2016) will be studied. Another difference concerns the Schmidt number $Sc = \nu/D$, where ν is the viscosity and D the diffusivity. Leclercq *et al.* (2016) use $Sc = 700$ while we shall set $Sc = 1$ herein.

This study will be completed by an analysis of linear transient growth mechanisms in the linearly stable regime of the Froude–Reynolds numbers parameter space. The linear transient growth of the Taylor–Couette flow has been first investigated in homogeneous fluids by Hristova *et al.* (2002) and Meseguer (2002) owing to its potential importance in explaining subcritical transition to turbulence (Schmid & Henningson 2001). Hristova *et al.* (2002) studied the effects of the Reynolds number and the gap ratio η on axisymmetric perturbations for a given axial wavelength $\lambda_z = 2(r_o - r_i)$ and for exact counter-rotation of the cylinders, $\mu = -1$. They found that transient growth in this case can occur through the lift-up effect and it becomes identical to that of the plane Couette flow for η close to unity. Meseguer (2002) investigated the transient growth over wide ranges of inner and outer angular speeds and for various axial and azimuthal wavenumbers for a given small gap. He showed that non-axisymmetric perturbations can achieve larger transient growth than axisymmetric ones. More recently, Maretzke *et al.* (2014) studied thoroughly transient growths of the Taylor–Couette flow for various gap ratio η and angular velocity ratio μ covering all linearly stable regimes. They showed that non-axisymmetric perturbations lead to transient energy growth by the Orr mechanism. Their numerical results show that the maximum energy growth G_{max} scales with the Reynolds number as $G_{max} \sim Re_s^{2/3}$ where Re_s is the shear Reynolds number measuring the absolute shear in the flow. Maretzke *et al.* (2014) further explained this scaling in the case of two-dimensional perturbations with zero axial wavenumber by means of an asymptotic WKBJ analysis for large Re_s . The dominant transient growth mechanism for the Taylor–Couette flow in non-Newtonian fluids has been also recently investigated (Agbessi *et al.* 2015; Chen, Wan & Zhang 2015). In contrast, there exists no study on the linear transient growth of the Taylor–Couette flow in stratified fluids. Transient growth in stratified fluids has been studied only for parallel shear layers, either with horizontal shear (Bakas & Farrell 2009a,b; Arratia 2011) or with vertical shear (Farrell & Ioannou 1993; Bakas, Ioannou & Kefaliakos 2001; Kaminski, Caulfield & Taylor 2014). In the case of horizontal shear, optimal energy growth is achieved by three-dimensional perturbations through the Orr mechanism and the excitation of internal waves. The configuration with horizontal shear investigated by Arratia (2011) resembles closely to the stratified Taylor–Couette flow. An important difference, however, is that the shear layer is unstable to the normal-mode Kelvin–Helmholtz instability while we shall investigate here transient growth of the stratified Taylor–Couette viscous flow in the stable regime of the Froude–Reynolds numbers parameter space for exactly counter-rotating cylinders $\mu = -1$.

The paper is organized as follows. After having formulated the stability problem in §2, we focus in §§3 and 4 on the stability of the stratified Taylor–Couette flow for the angular velocity ratios $\mu = -1$ and $\mu = 0.5$ which are thought to be typical examples of the Rayleigh-unstable regimes of counter-rotation and co-rotation, respectively. The gap ratio will be fixed for $\eta = 0.9$ throughout the paper. We shall demonstrate that both the CI and SRI can appear and compete in these regimes.

To show this, numerical and asymptotic stability analyses are first performed in the inviscid and non-diffusive limits. Next, the dominant instability in presence of viscosity and diffusion is determined numerically as a function of the Reynolds number and the Froude number. In §5, transient growth is investigated when the stratified Taylor–Couette viscous flow is linearly stable for $\mu = -1$. The maximum energy growth and associated growth mechanism are determined over all axial and azimuthal wavenumbers as a function of the Reynolds and Froude numbers.

2. Problem formulation

2.1. Stability equations

We perform a linear stability analysis of the base flow (1.1) when there is a stable density stratification in the axial direction with a constant Brunt–Väisälä frequency $N = \sqrt{-(g/\rho_0)\partial\bar{\rho}/\partial z}$, where g is the gravity, ρ_0 is the reference density and $\bar{\rho}(z)$ is the basic density profile in the vertical direction z . To non-dimensionalize the problem, we use time scale $1/\Omega_o$ and length scale r_i . The pressure and density perturbations are non-dimensionalized by $\rho_0\Omega_o^2 r_i^2$ and $\rho_0 N^2 r_i/g$, respectively. For simplicity, the non-dimensional angular velocity and radius will be denoted Ω and r , i.e. with the same notation as the dimensional variables in (1.1). Under the Boussinesq approximation, the linearized non-dimensional momentum, continuity and density equations for the perturbations of velocity $(\tilde{u}_r, \tilde{u}_\theta, \tilde{u}_z)$, pressure \tilde{p} and density $\tilde{\rho}$ in cylindrical coordinates (r, θ, z) are

$$\frac{\partial \tilde{u}_r}{\partial t} = -\Omega \frac{\partial \tilde{u}_r}{\partial \theta} + 2\Omega \tilde{u}_\theta - \frac{\partial \tilde{p}}{\partial r} + \frac{1}{Re} \left[\tilde{\nabla}^2 \tilde{u}_r - \frac{\tilde{u}_r}{r^2} - \frac{2}{r^2} \frac{\partial \tilde{u}_\theta}{\partial \theta} \right], \quad (2.1)$$

$$\frac{\partial \tilde{u}_\theta}{\partial t} = -\Omega \frac{\partial \tilde{u}_\theta}{\partial \theta} - Z \tilde{u}_r - \frac{1}{r} \frac{\partial \tilde{p}}{\partial \theta} + \frac{1}{Re} \left[\tilde{\nabla}^2 \tilde{u}_\theta - \frac{\tilde{u}_\theta}{r^2} + \frac{2}{r^2} \frac{\partial \tilde{u}_r}{\partial \theta} \right], \quad (2.2)$$

$$\frac{\partial \tilde{u}_z}{\partial t} = -\Omega \frac{\partial \tilde{u}_z}{\partial \theta} - \frac{\partial \tilde{p}}{\partial z} - \frac{1}{F^2} \tilde{\rho} + \frac{1}{Re} \tilde{\nabla}^2 \tilde{u}_z, \quad (2.3)$$

$$\frac{1}{r} \frac{\partial (r \tilde{u}_r)}{\partial r} + \frac{1}{r} \frac{\partial \tilde{u}_\theta}{\partial \theta} + \frac{\partial \tilde{u}_z}{\partial z} = 0, \quad (2.4)$$

$$\frac{\partial \tilde{\rho}}{\partial t} = -\Omega \frac{\partial \tilde{\rho}}{\partial \theta} + \tilde{u}_z + \frac{1}{Re Sc} \tilde{\nabla}^2 \tilde{\rho}, \quad (2.5)$$

where $Z = (1/r)(\partial/\partial r)(r^2\Omega)$ is the axial vorticity of the base flow, $\tilde{\nabla}^2 = \partial^2/\partial r^2 + (1/r)(\partial/\partial r) + (1/r^2)(\partial^2/\partial \theta^2) + \partial^2/\partial z^2$ the Laplacian operator, $F = \Omega_o/N$ the Froude number, $Re = \Omega_o r_i^2/\nu$ the Reynolds number and $Sc = \nu/D$ the Schmidt number, with ν the viscosity and D the diffusivity. The Schmidt number will be set to unity throughout the paper. Writing the perturbations in the form of normal modes as

$$(\tilde{u}_r, \tilde{u}_\theta, \tilde{u}_z, \tilde{p}, \tilde{\rho}) = (u_r(r), u_\theta(r), u_z(r), p(r), \rho(r))e^{i(kz+m\theta-\omega t)} + \text{c.c.}, \quad (2.6)$$

where k is the vertical wavenumber, m is the azimuthal wavenumber, ω is the complex frequency with $\omega = \omega_r + i\omega_i$ where ω_r is the frequency and ω_i is the growth rate, and c.c. denotes the complex conjugate, equations (2.1)–(2.5) become:

$$i(-\omega + m\Omega)u_r = 2\Omega u_\theta - \frac{dp}{dr} + \frac{1}{Re} \left[\nabla^2 u_r - \frac{u_r}{r^2} - \frac{2im}{r^2} u_\theta \right], \quad (2.7)$$

$$i(-\omega + m\Omega)u_\theta = -Zu_r - \frac{imp}{r} + \frac{1}{Re} \left[\nabla^2 u_\theta - \frac{u_\theta}{r^2} + \frac{2im}{r^2} u_r \right], \quad (2.8)$$

$$i(-\omega + m\Omega)u_z = -ikp - \frac{1}{F^2} \rho + \frac{1}{Re} \nabla^2 u_z, \quad (2.9)$$

$$\frac{1}{r} \frac{d(ru_r)}{dr} + \frac{imu_\theta}{r} + iku_z = 0, \quad (2.10)$$

$$i(-\omega + m\Omega)\rho = u_z + \frac{1}{Re Sc} \nabla^2 \rho, \quad (2.11)$$

where $\nabla^2 = d^2/dr^2 + (1/r)(d/dr) - (k^2 + m^2/r^2)$ is the Laplacian operator in modal form. Because of the symmetry $\omega(k, m) = \omega(-k, m) = -\omega^*(-k, -m)$ where $*$ denotes the complex conjugate, we can only consider non-negative k and m . Equations (2.7)–(2.11) can be reduced to three equations with variables u_r , u_θ and ρ in the form

$$(-i\omega)\mathbf{B}\mathbf{v} = \mathbf{A}\mathbf{v}, \quad (2.12)$$

where $\mathbf{v} = (u_r, u_\theta, \rho)^T$, T denotes the matrix transpose and \mathbf{A} and \mathbf{B} are 3×3 differential operator matrices (see Park (2012) for the detailed expressions of \mathbf{A} and \mathbf{B}). The eigenvalue problem (2.12) is solved numerically by the Chebyshev collocation spectral method (Antkowiak 2005). The number of collocation points used in the radial direction is between 80 and 120.

In the inviscid and non-diffusive limits (i.e. $\nu = D = 0$), (2.7)–(2.11) can be reduced to a single equation for $u_r(r)$

$$\frac{d^2 u_r}{dr^2} + \left(\frac{1}{r} - \frac{Q'}{Q} \right) \frac{du_r}{dr} + \left[k^2 \beta - \frac{m^2}{r^2} - \frac{mrQ}{s} \left(\frac{Z}{r^2 Q} \right)' + Q \left(\frac{1}{rQ} \right)' \right] u_r(r) = 0, \quad (2.13)$$

where $s(r) = -\omega + m\Omega$ is the Doppler-shifted frequency, $Q(r) = m^2/r^2 - k^2 s^2/(1/F^2 - s^2)$, $\beta(r) = (s^2 - \phi)/(1/F^2 - s^2)$, $\phi(r) = 2Z\Omega$ is the Rayleigh discriminant and prime denotes the differentiation with respect to r (Billant & Le Dizès 2009; Le Dizès & Billant 2009; Park & Billant 2012).

2.2. Transient growth

Transient growth of perturbations will be investigated in the regimes that are linearly stable according to the previous modal stability analysis. To this end, we consider the total energy of the perturbations defined as

$$E(t) = \frac{1}{2} \int_1^{1/\eta} \left(|\hat{u}_r|^2 + |\hat{u}_\theta|^2 + |\hat{u}_z|^2 + \frac{1}{F^2} |\hat{\rho}|^2 \right) r dr, \quad (2.14)$$

where $|u|^2 = u^* u$ and the perturbations are no longer written in terms of a single frequency:

$$(\tilde{u}_r, \tilde{u}_\theta, \tilde{u}_z, \tilde{\rho}) = (\hat{u}_r(r, t), \hat{u}_\theta(r, t), \hat{u}_z(r, t), \hat{\rho}(r, t)) e^{i(kz + m\theta)} + \text{c.c.} \quad (2.15)$$

This can be expressed in terms of $\hat{\mathbf{v}} = (\hat{u}_r, \hat{u}_\theta, \hat{\rho})^T$ and $\hat{\mathbf{q}} = (\hat{u}_r, \hat{u}_\theta, \hat{u}_z, \hat{\rho}/F)^T \equiv \mathbf{P}\hat{\mathbf{v}}$ where \mathbf{P} is the operator transforming $\hat{\mathbf{v}}$ into $\hat{\mathbf{q}}$,

$$E(t) = \frac{1}{2} \int_1^{1/\eta} \hat{\mathbf{q}}^\dagger \hat{\mathbf{q}} r dr = \frac{1}{2} \int_1^{1/\eta} \hat{\mathbf{v}}^\dagger \mathbf{P}^\dagger \mathbf{P} \hat{\mathbf{v}} r dr \equiv \|\hat{\mathbf{v}}(t)\|_E, \quad (2.16)$$

where the superscript \dagger denotes the Hermitian. Rewriting the (2.12) as an evolution equation

$$\frac{\partial \hat{\mathbf{v}}}{\partial t} = \mathbf{L} \hat{\mathbf{v}}, \quad (2.17)$$

where $\mathbf{L} = \mathbf{B}^{-1} \mathbf{A}$, the solution can be expressed as $\hat{\mathbf{v}}(t) = \exp(t\mathbf{L}) \hat{\mathbf{v}}(0)$. The optimal energy growth $G(t)$ is then defined as

$$G(t) \equiv \max_{\hat{\mathbf{v}}(0)} \frac{\mathbf{E}(t)}{\mathbf{E}(0)} = \max_{\hat{\mathbf{v}}(0)} \frac{\|\hat{\mathbf{v}}(t)\|_E}{\|\hat{\mathbf{v}}(0)\|_E} = \max_{\hat{\mathbf{v}}(0)} \frac{\|\exp(t\mathbf{L}) \hat{\mathbf{v}}(0)\|_E}{\|\hat{\mathbf{v}}(0)\|_E} = \|\exp(t\mathbf{L})\|_E. \quad (2.18)$$

To compute the optimal energy growth $G(t)$ and the maximum optimal energy growth $G_{\max} = \max_{t \geq 0} G(t)$, we use the eigenvector expansion method (Schmid & Henningson 2001). We decompose $\hat{\mathbf{v}}$ into the first N_e least stable eigenvectors $\hat{\mathbf{v}}_n$ of \mathbf{L} as

$$\hat{\mathbf{v}}(r, t) = \sum_{n=1}^{N_e} \kappa_n(t) \hat{\mathbf{v}}_n(r), \quad (2.19)$$

where $\kappa_n(t)$ is the expansion coefficient satisfying

$$\frac{d\kappa}{dt} = \mathbf{A} \kappa, \quad (2.20)$$

where $\kappa = (\kappa_1, \dots, \kappa_{N_e})^T$ and $\mathbf{A} = \text{diag}(-i\omega_1, \dots, -i\omega_{N_e})$ with the N_e least stable eigenvalues. Then the total energy of perturbations becomes

$$\mathbf{E}(t) = \|\hat{\mathbf{v}}\|_E = \frac{1}{2} \int_1^{1/\eta} \left(\sum_{i=1}^{N_e} \kappa_i \hat{\mathbf{v}}_i \right)^\dagger \mathbf{P}^\dagger \mathbf{P} \left(\sum_{j=1}^{N_e} \kappa_j \hat{\mathbf{v}}_j \right) r dr = \sum_{i=1}^{N_e} \sum_{j=1}^{N_e} \kappa_i^* \mathcal{M}_{ij} \kappa_j, \quad (2.21)$$

where

$$\mathcal{M}_{ij} = \frac{1}{2} \int_1^{1/\eta} \hat{\mathbf{v}}_i^\dagger \mathbf{P}^\dagger \mathbf{P} \hat{\mathbf{v}}_j r dr. \quad (2.22)$$

Applying the Cholesky factorization $\mathcal{M} = \mathbf{F}^\dagger \mathbf{F}$, we obtain finally the expression of the optimal transient energy growth in terms of the L_2 norm:

$$G(t) = \max_{\kappa(0)} \frac{\kappa^\dagger(t) \mathbf{F}^\dagger \mathbf{F} \kappa(t)}{\kappa^\dagger(0) \mathbf{F}^\dagger \mathbf{F} \kappa(0)} = \max_{\kappa(0)} \frac{\|\mathbf{F} \kappa(t)\|_2^2}{\|\mathbf{F} \kappa(0)\|_2^2} = \max_{\kappa(0)} \frac{\|\mathbf{F} e^{t\mathbf{A}} \kappa(0)\|_2^2}{\|\mathbf{F} \kappa(0)\|_2^2} = \|\mathbf{F} \exp(t\mathbf{A}) \mathbf{F}^{-1}\|_2^2. \quad (2.23)$$

The last quantity in the right-hand side of (2.23) is the square of the largest singular value of $\mathbf{F} \exp(t\mathbf{A}) \mathbf{F}^{-1}$ which can be computed via the singular value decomposition (Schmid & Henningson 2001). The number of least stable eigenvectors N_e used to compute $G(t)$ and G_{\max} is between 40 and 60. This is sufficient to obtain converged values of $G(t)$ and G_{\max} . The numerical code has been validated against previous results in homogeneous fluids (i.e. $1/F = 0$). For example, for $Re_i = 591$, $\mu = -3.8579$ and $\eta = 0.881$, Meseguer (2002) found $G_{\max} = 71.36$ at $m = 10$ and $k = 1.994$, and Maretzke *et al.* (2014) found $G_{\max} = 71.58$ at $m = 10$ and $k = 1.997$ while our code yields $G_{\max} = 71.5851$ at $m = 10$ and $k = 1.997$. We have tested other sets of parameters and an excellent agreement with Hristova *et al.* (2002) and Maretzke *et al.* (2014) has always been found.

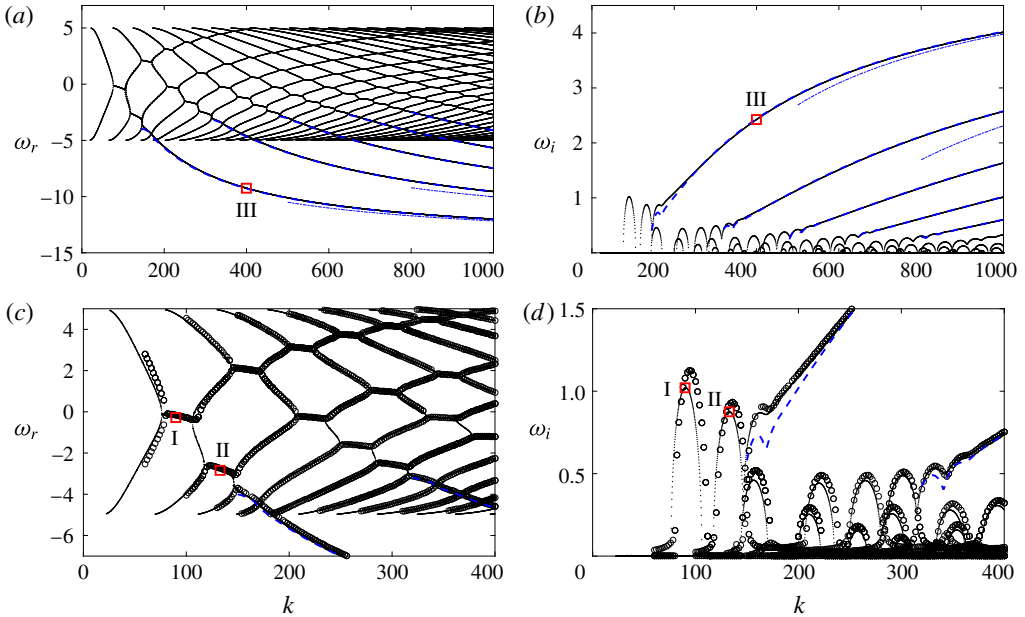


FIGURE 1. (Colour online) (a) Frequency and (b) growth rate as a function of axial wavenumber k for $m=15$, $F=1/20$, $\mu=-1$ and $\eta=0.9$ in the inviscid and non-diffusive limits. (c,d) Same as (a,b) but zoomed in on the wavenumber range $k \leq 400$. Numerical results obtained by solving (2.7) are indicated by dots. The different asymptotic results are shown by: blue dashed lines, (3.7); blue dash-dotted lines, (3.10); empty circles, (3.16). Square symbols indicate eigenvalues of the eigenmodes I, II and III displayed in figure 2.

3. Instabilities in the regime of counter-rotation

In this section, we study the instabilities in the case of exact counter-rotation $\mu = -1$ which will serve as a typical example of the Rayleigh-unstable regime $\mu < 0$. The Rayleigh-unstable regime of co-rotation $0 \leq \mu < \eta^2$, which is slightly different, will be investigated in §4. We first focus on the inviscid and non-diffusive limits in §§3.1–3.4, while viscous effects will be considered in §3.5.

3.1. Typical example

Figure 1 shows a typical example of frequency ω_r and growth rate ω_i as a function of axial wavenumber k in the inviscid and non-diffusive limits for $m=15$, $F=1/20$ and $\mu=-1$. As mentioned before, the gap ratio will be set to $\eta=0.9$ throughout the paper. There are only few branches in the frequency range $\omega_r < -5$ but their corresponding growth rates are large and increase monotonically as k increases. These behaviours are reminiscent of the CI observed in vortices (Smyth & McWilliams 1998; Billant & Gallaire 2005; Park & Billant 2013a). However, many growth rate peaks are present at finite wavenumbers. They occur when two frequency branches, one descending from $\omega_r = 5$ and the other ascending from $\omega_r = -5$, cross and become locked. These two types of frequency branches correspond to inertia-gravity waves trapped near the inner and outer cylinders. The origin of the particular limits $\omega_r = \pm 5$ will be explained in §3.2. The instability due to the resonance of these waves is the SRI (Molemaker *et al.* 2001; Le Bars & Le Gal 2007; Park & Billant 2013b). Therefore, the CI and

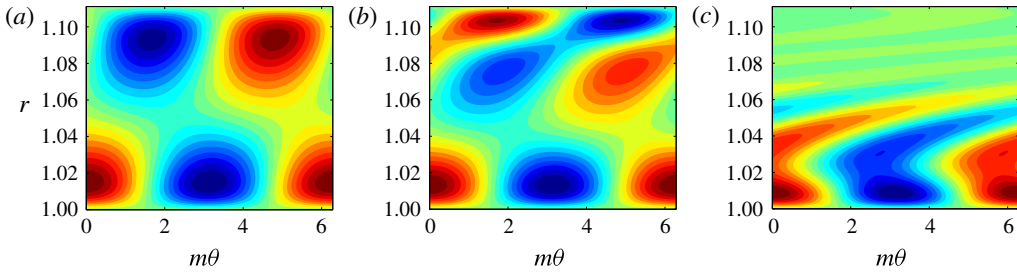


FIGURE 2. (Colour online) Contour plots of the real part of the eigenfunction $\text{Re}[u_r(r) \exp(im\theta)]$ in the plane (r, θ) for (a) mode I: $k = 90$, $\omega = -0.270 + 1.021i$, (b) mode II: $k = 133$, $\omega = -2.835 + 0.876i$, (c) mode III: $k = 400$, $\omega = -9.249 + 2.425i$. The other parameters are the same as in figure 1. The contours are normalized by the maximum value of u_r and the contour interval is 0.1.

SRI co-exist but can be clearly distinguished from their frequency and growth rate behaviours as a function of the axial wavenumber k .

These two instabilities have also distinct eigenfunctions. Figure 2 shows examples of the eigenfunction u_r for (a) $k = 90$ and $\omega = -0.270 + 1.021i$ corresponding to the first peak of resonance of the SRI (indicated by I in figure 1), for (b) $k = 133$ and $\omega = -2.835 + 0.876i$ corresponding to the second peak of the SRI (indicated by II), and for (c) $k = 400$ and $\omega = -9.249 + 2.425i$ belonging to the first branch of the CI (indicated by III). We see that the SRI and CI modes have very different shapes. The first SRI mode (figure 2a) consists of two waves trapped near the inner and outer cylinders with a phase shift and similar amplitudes, as observed by Yavneh *et al.* (2001) and Park & Billant (2013b). The second SRI mode (figure 2b) is similar except that the wave trapped near the outer cylinder exhibits an additional node because this mode is due to the resonance of the second lower branch with the first upper branch (figure 1). In contrast, the CI mode (figure 2c) has a large amplitude near the inner cylinder for $r \lesssim 1.06$ and exhibits weak sheared waves for $r \gtrsim 1.06$. The radius $r \approx 1.06$ which divides these two regions corresponds approximately to the radius $r_0 = 1.051$ above which the Rayleigh discriminant becomes positive (i.e. $\phi(r_0) = 0$). In the following section, we shall confirm these different characteristics of the CI and SRI by means of a WKBJ analysis.

3.2. The WKBJ approximation

For large k , the equation (2.13) can be approximated by

$$\frac{d^2 u_r}{dr^2} + \left(\frac{1}{r} - \frac{Q'}{Q} \right) \frac{du_r}{dr} + [k^2 \beta + O(1)] u_r(r) = 0, \quad (3.1)$$

and we can obtain an asymptotic solution of (3.1) by means of the WKBJ approximation:

$$u_r = \frac{Q^{1/2}}{r^{1/2} \beta^{1/4}} \left[A_+ \exp \left(ik \int_{r_{t1}}^r \sqrt{\beta(t)} dt \right) + A_- \exp \left(-ik \int_{r_{t1}}^r \sqrt{\beta(t)} dt \right) \right], \quad (3.2)$$

where A_{\pm} are constants and r_{t1} is a turning point where $\beta(r_{t1}) = 0$ (Bender & Orszag 1978). As a first step, we assume for simplicity that the growth rate ω_i is zero so that

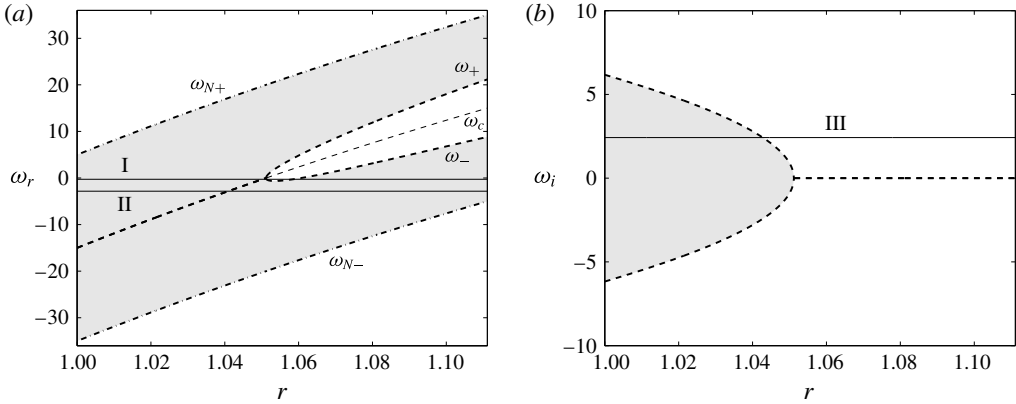


FIGURE 3. (a) Real part of epicyclic frequencies ω_{\pm} (thick dashed lines) and $\omega_{N\pm}$ (thick dash-dotted lines), and critical frequency ω_c (thin dashed line) for $m = 15$, $F = 1/20$, $\mu = -1$ and $\eta = 0.9$. β is positive in the shaded regions. The solid lines I and II indicate the frequency ω_r of the eigenmodes shown in figure 2(a,b). (b) Imaginary part of epicyclic frequencies ω_{\pm} (dashed lines). The solid line III indicates the growth rate ω_i of the eigenmode shown in figure 2(c).

β is purely real. Depending on the sign of $\beta(r)$, the WKB approximation (3.2) is wavelike ($\beta > 0$) or exponential ($\beta < 0$). In order to easily figure out the sign of $\beta(r)$ for a given real frequency ω , it is convenient to introduce the epicyclic frequencies $\omega_{\pm}(r) = m\Omega \pm \sqrt{\phi}$ and critical frequencies $\omega_{N\pm} = m\Omega \pm 1/F$ (Le Dizès & Lacaze 2005). Then, we can write

$$\beta = -\frac{(\omega - \omega_+)(\omega - \omega_-)}{(\omega - \omega_{N+})(\omega - \omega_{N-})}. \quad (3.3)$$

When the Froude number is sufficiently small so that $\text{Re}(\omega_+) < \omega_{N+}$ and $\omega_{N-} < \text{Re}(\omega_-)$, the expression (3.3) shows that β is positive if the frequency ω_r lies in ranges $\text{Re}(\omega_+) < \omega_r < \omega_{N+}$ or $\omega_{N-} < \omega_r < \text{Re}(\omega_-)$, and negative elsewhere as seen in the example displayed in figure 3(a). The critical frequency $\omega_c = m\Omega$ is also plotted in figure 3(a). We can see that the real part of the epicyclic frequencies $\text{Re}(\omega_{\pm})$ and the critical frequency ω_c merge at $r = r_0 = \sqrt{(1 - \mu)/(\eta^2 - \mu)}$ because $\phi(r)$ is negative for $r < r_0$.

Non-singular inertia gravity waves, i.e. without the presence of critical points $r_{N\pm}$ where $\omega_r = \omega_{N\pm}$, can exist if their frequency lies in the interval $\max(\omega_{N-}) < \omega_r < \min(\omega_{N+})$. This corresponds to $-5 < \omega_r < 5$ for $m = 15$ and $F = 1/20$ explaining the frequency range of most of the branches in figure 1(a), excepted those corresponding to the CI. The SRI can exist if there are two wave regions at a given frequency separated by the critical frequency ω_c (Park & Billant 2013b). When the epicyclic and critical frequencies increase with r as in figure 3(a) (i.e. when $\mu < 0$ or $\mu > 1$), the conditions for the existence of the SRI are therefore: $\min(\omega_{N+}) > \max(\omega_{N-})$, $\max(\text{Re}(\omega_-)) > \max(\omega_{N-})$, $\min(\omega_{N+}) > \min(\text{Re}(\omega_+))$ and $\max(\text{Re}(\omega_-)) > \min(\text{Re}(\omega_+))$. These conditions for the SRI lead to the following relations when $\mu < 0$:

$$\frac{1}{F} > \max \left[\frac{m}{2} \left(1 - \frac{1}{\mu} \right), 2\sqrt{\frac{1 - \eta^2/\mu}{1 - \eta^2}} \right], \quad m > \frac{-2\mu}{1 - \mu} \sqrt{\frac{1 - \eta^2/\mu}{1 - \eta^2}}. \quad (3.4a,b)$$

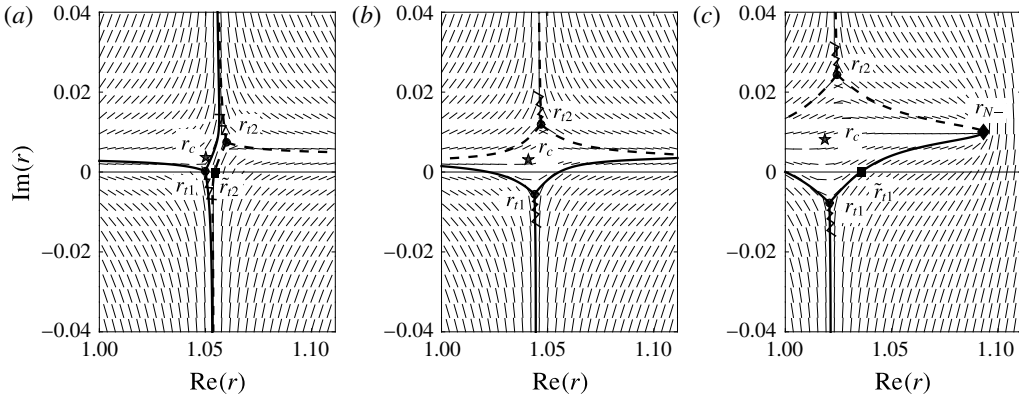


FIGURE 4. Stokes line networks for (a) $\omega = -0.270 + 1.021i$, (b) $\omega = -2.835 + 0.876i$ and (c) $\omega = -9.249 + 2.425i$, corresponding to the modes I, II and III shown in figure 2, respectively. The other parameters are the same as in figure 1. Thick solid and dashed lines are the Stokes lines emitted from the turning points r_{t1} and r_{t2} (dots), respectively. Short lines indicate the direction of $\text{Re}(\int_{r_i}^r \sqrt{-\beta(t)} dt) = \text{const.}$, and wavy lines indicate the branch cuts. The critical points r_c and r_{N-} are indicated by star and diamond symbols, respectively. The square symbols represent the radii at which Stokes lines cross the real axis.

These conditions imply that the SRI can occur only when the stratification is sufficiently strong and when the azimuthal wavenumber is sufficiently large. They are satisfied for the examples of frequency indicated by the lines I and II in figure 3(a).

In the case of the CI, the growth rate is not small and it is therefore not appropriate to consider a real frequency as in figure 3(a). In a first approach, it is convenient to assume instead that the frequency is $\omega_r = m\Omega$ and consider an arbitrary growth rate ω_i . In this case, β is also purely real. As seen in figure 3(b), β is then positive close to the inner cylinder when $-\max(\sqrt{-\phi}) < \omega_i < \max(\sqrt{-\phi})$. For the growth rate indicated by the line I, the WKBJ approximations are wavelike between the inner cylinder r_i and a turning point r_{t1} , and exponential for $r > r_{t1}$.

The above descriptions of the sign of β for the SRI and CI have assumed that β is purely real for simplicity. For the SRI, ω has been assumed to be purely real despite that the growth rate ω_i is non-zero. Conversely, for the CI, the frequency has been assumed to be $\omega_r = m\Omega$ even if ω_r should be constant. When these assumptions are abandoned, β is complex meaning that the WKBJ analysis should be performed in the complex plane. This is the purpose of the next sections.

3.3. Complex WKBJ analysis for the CI

Figure 4(c) shows the Stokes line networks in the complex r -plane for the eigenvalues $\omega = -9.249 + 2.425i$ corresponding to the CI mode shown in figure 2(c). There exist two turning points r_{t1} and r_{t2} with $\text{Re}(r_{t1}) < \text{Re}(r_{t2})$. The critical point r_{N-} where $\omega = \omega_{N-}$ can be also seen in figure 4(c). The thick lines show the Stokes lines which satisfy $\text{Re}(\int_{r_i}^r \sqrt{-\beta}) = 0$. They divide the complex plane into domains where the WKBJ approximations have the same exponential behaviours (Olver 1974). We see in figure 4(c) that only one of the three Stokes lines emanating from r_{t1} crosses the real axis at \tilde{r}_{t1} (indicated by a square symbol). Such structure is similar to the one studied in homogeneous fluids by Billant & Gallaire (2005). We first assume that the

WKB approximation (3.2) is valid for $r_i < r < \tilde{r}_{t1}$. In order to find the matching WKB approximation for $r > \tilde{r}_{t1}$, we need to consider the vicinity of the turning point r_{t1} where (3.2) is no longer valid. An approximation of (2.13) around r_{t1} is Airy's equation:

$$\frac{d^2 u_r}{d\tilde{r}^2} - \tilde{r} u_r = O(\epsilon), \quad (3.5)$$

where $\tilde{r} = (r - r_{t1})/\epsilon$ and $\epsilon = 1/[-\beta'(r_{t1})k^2]^{1/3}$. Matching the asymptotic behaviour of Airy's function from $\tilde{r} \rightarrow -\infty$ (with $|\arg(-\tilde{r})| < 2\pi/3$) to $\tilde{r} \rightarrow \infty$ (with $|\arg(\tilde{r})| < \pi$) (Abramowitz & Stegun 1965) shows that the WKB approximation in the range $\tilde{r}_{t1} < r < r_o$ which matches (3.2) is

$$u_r = \frac{Q^{1/2} e^{-i\pi/4}}{r^{1/2} (-\beta)^{1/4}} \left[B_+ \exp \left(-k \int_{r_{t1}}^r \sqrt{-\beta(t)} dt \right) + B_- \exp \left(k \int_{r_{t1}}^r \sqrt{-\beta(t)} dt \right) \right], \quad (3.6)$$

where $B_+ = (A_+ + iA_-)/2$ and $B_- = iA_+ + A_-$. By imposing the boundary condition $u_r = 0$ at $r = r_i$ and $r = r_o$, we obtain the following dispersion relation

$$\frac{i - \exp \left(-2ik \int_{r_i}^{r_{t1}} \sqrt{\beta} dt \right)}{1 - i \exp \left(-2ik \int_{r_i}^{r_{t1}} \sqrt{\beta} dt \right)} + \frac{1}{2} \exp \left(-2k \int_{r_{t1}}^{r_o} \sqrt{-\beta} dt \right) = 0. \quad (3.7)$$

It can be further simplified at leading order in k to

$$k \int_{r_i}^{r_{t1}} \sqrt{\beta(t)} dt = \left(n - \frac{1}{4} \right) \pi, \quad (3.8)$$

where n is a positive integer. This implies that $\text{Im}(\int_{r_i}^{r_{t1}} \sqrt{\beta(t)} dt) = \text{Re}(\int_{r_i}^{r_{t1}} \sqrt{-\beta(t)} dt) = 0$ so that the turning point r_{t1} and the radius $r = r_i$ are connected by a Stokes line as observed in figure 4(c). Moreover, r_{t1} should be close to r_i in order to satisfy (3.8) as $k \rightarrow \infty$. Thus, we can Taylor expand β around r_i : $\beta(r) = \beta(r_i) + (r - r_i)\beta'(r_i) + O((r - r_i)^2)$. Then, (3.8) becomes

$$k \frac{(\beta(r_i))^{3/2}}{\beta'(r_i)} = -\frac{3}{2} \left(n - \frac{1}{4} \right) \pi, \quad (3.9)$$

which implies that $\beta(r_i)$ becomes zero as $k \rightarrow \infty$. By using the expansion $\omega = \omega_0 + \omega_1 k^{-2/3} + \dots$, ω can be obtained explicitly in terms of k as

$$\omega = m\Omega + i\sqrt{-\phi} - \frac{i(1/F^2 - \phi)}{2k^{2/3}\sqrt{-\phi}} \left[\frac{3\pi}{2} \left(n - \frac{1}{4} \right) \left(\frac{2im\sqrt{-\phi}\Omega' + \phi'}{1/F^2 - \phi} \right) \right]^{2/3} + \dots, \quad (3.10)$$

where all the variables are evaluated at $r = r_i$. When $F \rightarrow \infty$, this dispersion relation recovers the one obtained by Billant & Gallaire (2005) in homogeneous fluids. The asymptotic formula (3.7) and (3.10) are plotted in figure 1 with dashed lines and dash-dot lines, respectively. The formula (3.7) is almost identical to the numerical results and (3.10) is also in good agreement for large k . When the turning point r_{t1} is close to r_i , we could also directly apply the boundary condition $u_r = 0$ at $r = r_i$ to the solution of the local equation (3.5). This leads to a relation identical to (3.9) at leading order in k except that the right-hand side is replaced by $(-a_n)^{3/2}$ where a_n are the zeroes of the Airy function Ai . However, the differences between the zeroes a_n and the values of $((3\pi/8)(4n - 1))^{2/3}$ are at most 0.01 (see Billant & Gallaire 2005) so that the results are almost identical to those of (3.9).

3.4. Complex WKBJ analysis for the SRI

Similarly, figure 4(a) shows the Stokes line network for the eigenvalue $\omega = -0.270 + 1.021i$ of the SRI eigenmode shown in figure 2(a). There exist two turning points r_{t1} and r_{t2} which are close to the real axis. One Stokes line emanating from each turning point crosses the real axis. There are therefore three distinct regions on the real axis in contrast to the CI (figure 4c) where only two regions are present. Such configuration reflects the fact that the SRI consists physically in the resonance of two inertia–gravity waves trapped near each cylinder. This differs from the CI whose eigenmode is oscillatory only in a single region bounded by one cylinder. Another example of a Stokes line network is displayed in figure 4(b) for the second most unstable SRI mode (figure 2b). At first sight, this Stokes line network seems similar to the CI’s one (figure 4c). However, a crucial difference is that there are still two Stokes lines crossing the real axis thereby dividing the structure of the mode into three distinct regions instead of two for the CI. Park & Billant (2013b) have performed a matching analysis of the different WKBJ approximations for the SRI when the turning points are well separated. In figures 4(a,b), the two turning points are too close to each other for their analysis to be quantitatively valid. Since the turning points are close to the critical point r_c where $\omega = m\Omega(r_c)$, we can consider the local equation around r_c :

$$\frac{d^2 u_r}{d\tilde{r}_c^2} + (\tilde{r}_c^2 + \tilde{a}) u_r = O(\epsilon_c), \quad (3.11)$$

where $\tilde{r}_c = (r - r_c)/\epsilon_c$, $\epsilon_c = (km\Omega'(r_c)F)^{-1/2}$ and $\tilde{a} = -\phi(r_c)/(\epsilon_c m\Omega'(r_c))^2$. Note that \tilde{a} is positive if $\phi(r_c) < 0$ meaning that the two turning points $\tilde{r}_c = \pm i\sqrt{\tilde{a}}$ are in the complex plane (as in figure 4b) instead of being on the real axis. The solution of (3.11) is

$$u_r(\tilde{r}_c) = \tilde{r}_c e^{-(i/2)\tilde{r}_c^2} \left[c_1 M\left(\frac{3}{4} + \frac{i\tilde{a}}{4}, \frac{3}{2}, i\tilde{r}_c^2\right) + c_2 U\left(\frac{3}{4} + \frac{i\tilde{a}}{4}, \frac{3}{2}, i\tilde{r}_c^2\right) \right], \quad (3.12)$$

where c_1 and c_2 are constants and M and U denote the Kummer functions (Abramowitz & Stegun 1965). From the asymptotic behaviours of the Kummer functions from $\tilde{r}_c \rightarrow -\infty$ (with $|\arg(-\tilde{r}_c)| < \pi/2$) to $\tilde{r}_c \rightarrow \infty$ (with $|\arg(\tilde{r}_c)| < \pi/2$) (Abramowitz & Stegun 1965), we can obtain the WKBJ approximation in the range $\tilde{r}_{t2} < r < r_o$ which matches (3.2) in $r_i < r < \tilde{r}_{t1}$:

$$u_r = \frac{Q^{1/2}}{r^{1/2}\beta^{1/4}} \left[C_+ \exp\left(ik \int_{r_{t2}}^r \sqrt{\beta(t)} dt\right) + C_- \exp\left(-ik \int_{r_{t2}}^r \sqrt{\beta(t)} dt\right) \right], \quad (3.13)$$

where

$$C_+ = A_+ \left[\frac{2\pi \exp(-3\pi\tilde{a}/4) (4e/\tilde{a})^{-i\tilde{a}/2}}{\Gamma\left(\frac{3}{4} + \frac{i\tilde{a}}{4}\right) \Gamma\left(\frac{1}{4} + \frac{i\tilde{a}}{4}\right)} \right] - A_- \left[1 + \frac{2\pi \exp(\pi(3i - \tilde{a})/4)}{\Gamma\left(\frac{3}{4} - \frac{i\tilde{a}}{4}\right) \Gamma\left(\frac{1}{4} + \frac{i\tilde{a}}{4}\right)} \right], \quad (3.14)$$

$$C_- = -2A_- \left(\frac{4e}{\tilde{a}} \right)^{-i\tilde{a}/2} \frac{\Gamma\left(\frac{3}{4} + \frac{i\tilde{a}}{4}\right)}{\Gamma\left(\frac{3}{4} - \frac{i\tilde{a}}{4}\right)}$$

$$\times \left[\frac{-i\pi \exp(-\pi\tilde{a}/4)}{\Gamma\left(\frac{3}{4} - \frac{i\tilde{a}}{4}\right) \Gamma\left(\frac{1}{4} + \frac{i\tilde{a}}{4}\right)} + \exp\left(\frac{\pi(3i + 2\tilde{a})}{4}\right) \right] \\ + A_+ \left[1 + 2\pi \exp\left(\frac{\pi(3i - \tilde{a})}{4}\right) / \left\{ \Gamma\left(\frac{3}{4} - \frac{i\tilde{a}}{4}\right) \Gamma\left(\frac{1}{4} + \frac{i\tilde{a}}{4}\right) \right\} \right], \quad (3.15)$$

where Γ denotes the gamma function. Applying the boundary condition $u_r = 0$ at $r = r_i$ and $r = r_o$ leads to the dispersion relation

$$\exp\left(2ik \int_{r_{i2}}^{r_o} \sqrt{\beta(t)} dt\right) \left[\exp\left(2ik \int_{r_i}^{r_{i1}} \sqrt{\beta(t)} dt\right) \left\{ \frac{2\pi \exp(-3\pi\tilde{a}/4) (4e/\tilde{a})^{-i\tilde{a}/2}}{\Gamma\left(\frac{3}{4} + \frac{i\tilde{a}}{4}\right) \Gamma\left(\frac{1}{4} + \frac{i\tilde{a}}{4}\right)} \right\} \right. \\ \left. + 1 + \frac{2\pi \exp(\pi(3i - \tilde{a})/4)}{\Gamma\left(\frac{3}{4} - \frac{i\tilde{a}}{4}\right) \Gamma\left(\frac{1}{4} + \frac{i\tilde{a}}{4}\right)} \right] \\ + 2 \left(\frac{4e}{\tilde{a}}\right)^{-i\tilde{a}/2} \frac{\Gamma\left(\frac{3}{4} + \frac{i\tilde{a}}{4}\right)}{\Gamma\left(\frac{3}{4} - \frac{i\tilde{a}}{4}\right)} \left[\frac{-i\pi \exp(-\pi\tilde{a}/4)}{\Gamma\left(\frac{3}{4} - \frac{i\tilde{a}}{4}\right) \Gamma\left(\frac{1}{4} + \frac{i\tilde{a}}{4}\right)} + \exp\left(\frac{\pi(3i + 2\tilde{a})}{4}\right) \right] \\ + \exp\left(2ik \int_{r_{i1}}^{r_i} \sqrt{\beta(t)} dt\right) \left[1 + \frac{2\pi \exp(\pi(3i - \tilde{a})/4)}{\Gamma\left(\frac{3}{4} - \frac{i\tilde{a}}{4}\right) \Gamma\left(\frac{1}{4} + \frac{i\tilde{a}}{4}\right)} \right] = 0. \quad (3.16)$$

Since the asymptotic dispersion (3.16) is implicit, it has been solved by an iterative Newton method. As shown by the circle symbols in figure 1, it is in excellent agreement with the numerical results. Note that (3.16) also approximates very well the branches for which there is a transition from the SRI to the CI.

3.5. Effects of the Reynolds and Froude numbers

In this section, we investigate the effects of the Reynolds and Froude numbers for a Schmidt number fixed to $Sc = 1$. Figure 5(a) shows the growth rate as a function of k for $m = 15$, $F = 1/20$ and for different values of the Reynolds number: $Re_o = \Omega_o r_o (r_o - r_i)/\nu$. This is the usual definition of the Reynolds number for the Taylor–Couette flow (Andereck *et al.* 1986). It is related to the Reynolds number Re defined in § 2.1 by $Re_o = Re(1 - \eta)/\eta^2$. Both the CI and the SRI are stabilized as the Reynolds number decreases but the CI is stabilized faster than the SRI because the CI is most unstable for large k while the SRI exists in a finite range of moderate wavenumbers. For the parameters of figure 5(a), the SRI becomes more unstable than the CI for $Re_o < 11\,360$. The SRI remains unstable down to $Re_o \approx 2680$. Conversely, figure 5(b) shows the growth rate as a function of k for different Froude numbers for a fixed Reynolds number $Re_o = 10\,000$. When the Froude number is increased from $F = 1/20$ to $F = 1/10$, the SRI disappears because the condition (3.4) for its existence is

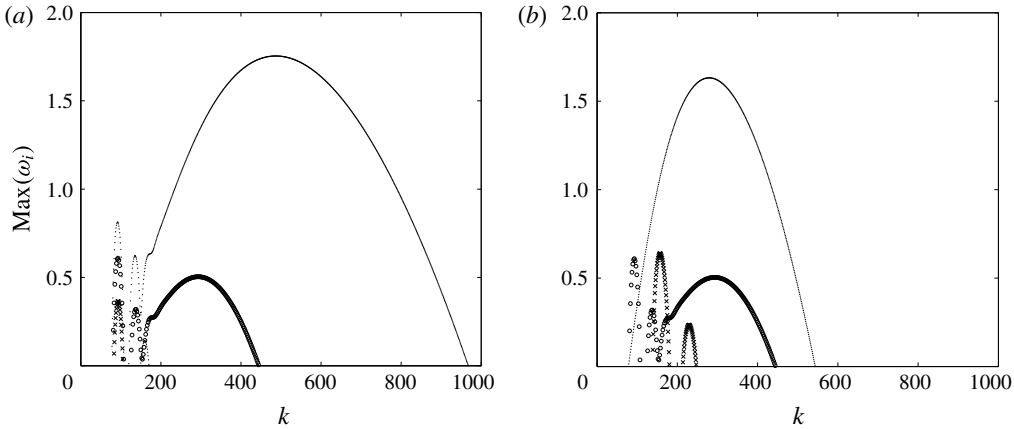


FIGURE 5. (a) Maximum growth rate $\max(\omega_i)$ as a function of the axial wavenumber k for $m=15$, $F=1/20$, $\mu=-1$, $\eta=0.9$, $Sc=1$ and for the Reynolds numbers $Re_o=30\,000$ (dot), $10\,000$ (empty circle) and 5000 (cross). (b) Maximum growth rate $\max(\omega_i)$ as a function of the axial wavenumber k for $Re_o=10\,000$ and for the Froude numbers $F=1/10$ (dot), $1/20$ (empty circle) and $1/30$ (cross). The other parameters are the same as in (a).

no longer satisfied. In contrast, the maximum growth rate of the CI increases. This is due to the fact that the number controlling viscous effects in strongly stratified fluids is the buoyancy Reynolds number $Re_{bo} = Re_o F^2$ because the inviscid stability equation (2.13) depends on k and F only through the similarity variable kF when $F \ll 1$ (Billant & Chomaz 2001). Hence, when the Froude number is increased from $F=1/20$ to $F=1/10$, Re_{bo} increases. Alternatively, when F is decreased to $F=1/30$ for $Re_o=10\,000$ (crosses in figure 5b), Re_{bo} decreases and the centrifugal instability is completely stabilized by viscous effects. In contrast, the SRI exists for $F=1/30$ since the condition (3.4) is satisfied.

Figure 6 shows the neutral stability curves of different azimuthal wavenumbers m in the parameter space $(1/F, Re_o)$. For weak stratification $1/F < 15$, the neutral Reynolds numbers grow with the stratification. In other words, the stratification stabilizes the CI as found by Boubnov *et al.* (1995) and Caton *et al.* (2000) for $\mu=0$. The overall neutral stability curve corresponds to the neutral stability curves for $m=3$ or 4 when $1/F < 15$, but they are almost identical to the one for $m=0$. The overall stability curve for $1/F < 15$ can be very well fitted to $Re_o \simeq 250.3 + 11.2/F^2$. This implies that the critical buoyancy Reynolds number is $Re_{bo} = 11.2 + 250.3F^2$.

On the other hand, when the stratification is stronger $1/F > 15$, the neutral Reynolds numbers Re_o decrease abruptly with $1/F$ when $m \geq 15$ (figure 6). The sudden transition occurs when the SRI starts to exist for a given azimuthal wavenumber m , i.e. when the condition (3.4) becomes satisfied. For $\mu=-1$, this occurs when $1/F \geq m$ as observed in figure 6. The critical Reynolds number for a given m reaches a minimum and then re-increases like $1/F^2$ as seen for $m=15$ in figure 6. The minimum critical Reynolds number is reached for larger $1/F$, i.e. stronger stratification as m increases. This is due to the fact that the vertical wavenumber k_c at which two waves resonate decreases as the azimuthal wavenumber increases. Thus, viscous effects due to the vertical shear, which scale like k_c^2/Re_o , decrease as the azimuthal wavenumber increases. However, for a fixed azimuthal wavenumber, the vertical wavenumber of the resonance scales like $k_c \sim 1/F$ for sufficiently small F

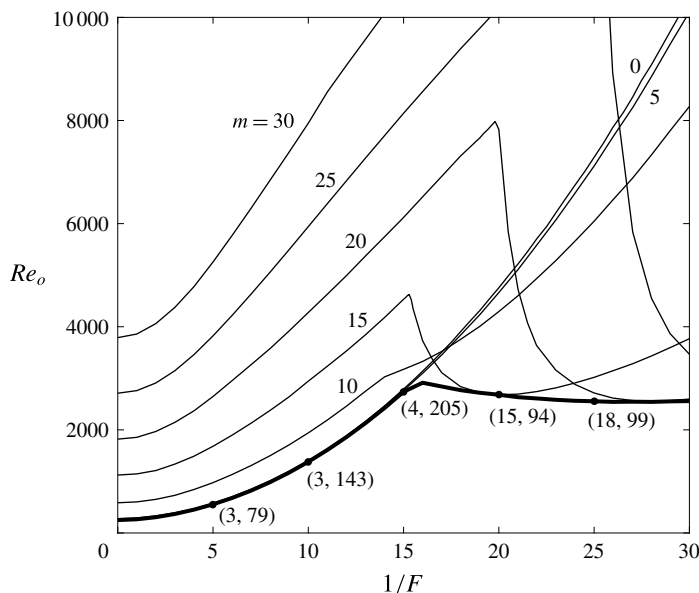


FIGURE 6. Neutral stability curves in the parameter space $(1/F, Re_o)$ for various azimuthal wavenumbers for $\mu = -1$, $\eta = 0.9$ and $Sc = 1$. The thick solid line represents the neutral stability curve for all azimuthal wavenumbers. The numbers (m_{max}, k_{max}) , indicated at a few selected points along this neutral curve, give the dominant azimuthal and axial wavenumbers m_{max}, k_{max} .

because of the self-similarity of strongly stratified fluids. Thus, vertical viscous effects increase like $1/(Re_o F^2)$ for large stratification for a given azimuthal wavenumber.

Because of these two effects, we see that the overall critical Reynolds number (bold solid line in figure 6) stabilizes at nearly a constant Reynolds number $Re_o \approx 2500$ when $1/F \geq 15$. Actually, it reaches a minimum at $1/F \approx 26$, $Re_o \approx 2540$, and then slowly increases for stronger stratification.

4. Instabilities in the regime of co-rotation $0 \leq \mu \leq \eta^2$

We now turn our attention to the value $\mu = 0.5$ which will serve as a typical example of the Rayleigh-unstable regime of co-rotation. The difference with negative angular velocity ratio $\mu < 0$ is that the epicyclic and critical frequencies $\omega_{\pm}, \omega_{N\pm}$ decrease with r since Ω decreases with r . In addition, the Rayleigh discriminant $\phi(r)$ is negative everywhere between the two cylinders. As in §3, we first present numerical and asymptotic results in the inviscid and non-diffusive limits in §§4.1–4.3, and viscous effects are then considered in §4.4.

4.1. Typical example

Figure 7 shows the frequency ω_r and growth rate ω_i as a function of k in the inviscid and non-diffusive limits for $m = 20$, $F = 1/20$, $\eta = 0.9$ and $\mu = 0.5$. Like for $\mu < 0$ in figure 1, the CI is most unstable in the limit $k \rightarrow \infty$. The beginning of the growth rate curves also exhibits peaks whenever two frequency branches of two wave families cross, which is the signature of the SRI. Figure 8(a) shows the eigenmode corresponding to the first peak of the SRI. Two out-of-phase waves near the inner

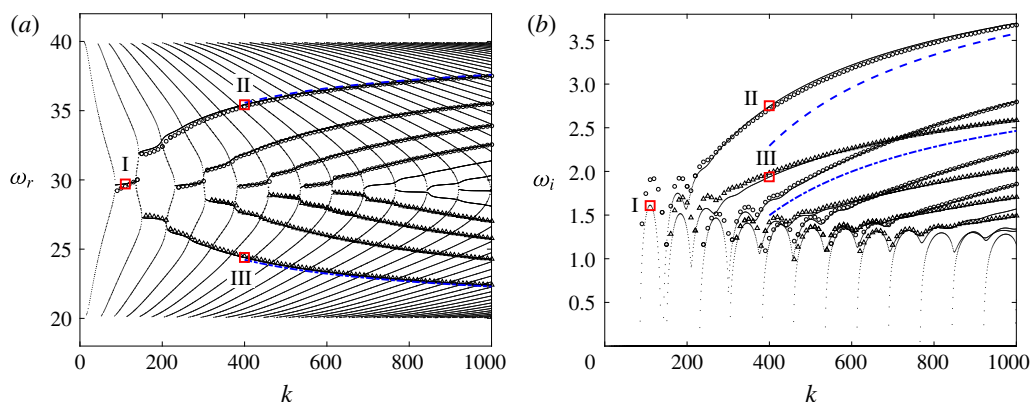


FIGURE 7. (Colour online) (a) Frequency and (b) growth rate as a function of axial wavenumber k for $m=20$, $F=1/20$, $\mu=0.5$ and $\eta=0.9$ in the inviscid and non-diffusive limits. Numerical results are indicated by dots, asymptotic results (4.2) and (4.5) are indicated by empty circles and empty triangles, and asymptotic results (3.10) with $n=1$ and (4.7) with $n_1=1$ are indicated by blue dashed lines and blue dash-dotted lines, respectively. Square symbols indicate the eigenvalues of the eigenmodes I, II and III shown in figure 8.

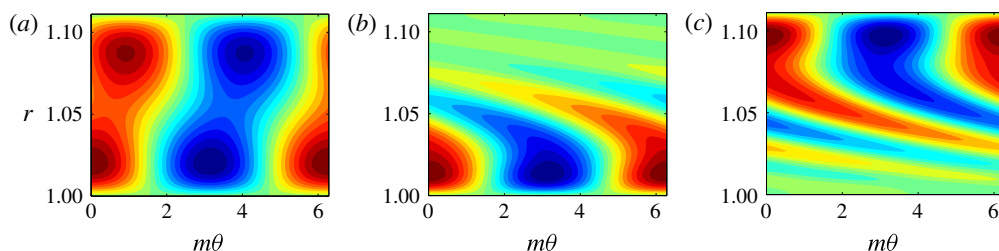


FIGURE 8. (Colour online) Contour plots of the real part of the eigenfunction $\text{Re}[u_r(r) \exp(im\theta)]$ in the plane $(m\theta, r)$ for (a) mode I: $k=110$, $\omega=29.72+1.61i$, (b) mode II: $k=400$, $\omega=35.43+2.75i$ and (c) mode III: $k=400$, $\omega=24.39+1.94i$. The parameters are the same as in figure 7. The contours are normalized by the maximum value of u_r , and the contour interval is 0.1.

and outer cylinders can be seen as for $\mu=-1$ (figure 2a). For larger wavenumber k , the growth rate increases monotonically and there is a smooth transition to the CI. A difference with the case $\mu=-1$ (figure 1) is that there are two types of CI branches, ones for which the frequency increases with k (referred to as upper branches hereafter) and the others for which the frequency decreases with k (lower branches). Interestingly, the growth rate of the upper branches increases faster with k than for the lower branches. Two examples of eigenmode corresponding to these two different branches are displayed in figure 8(b,c). As seen in figure 8(b), the eigenmode of the upper branch is concentrated near the inner cylinder like the one for $\mu=-1$ (figure 2c). In contrast, the eigenmode of the lower branch (figure 8c) is mostly localized near the outer cylinder, i.e. its structure is reversed compared to the eigenmode of the upper branch.

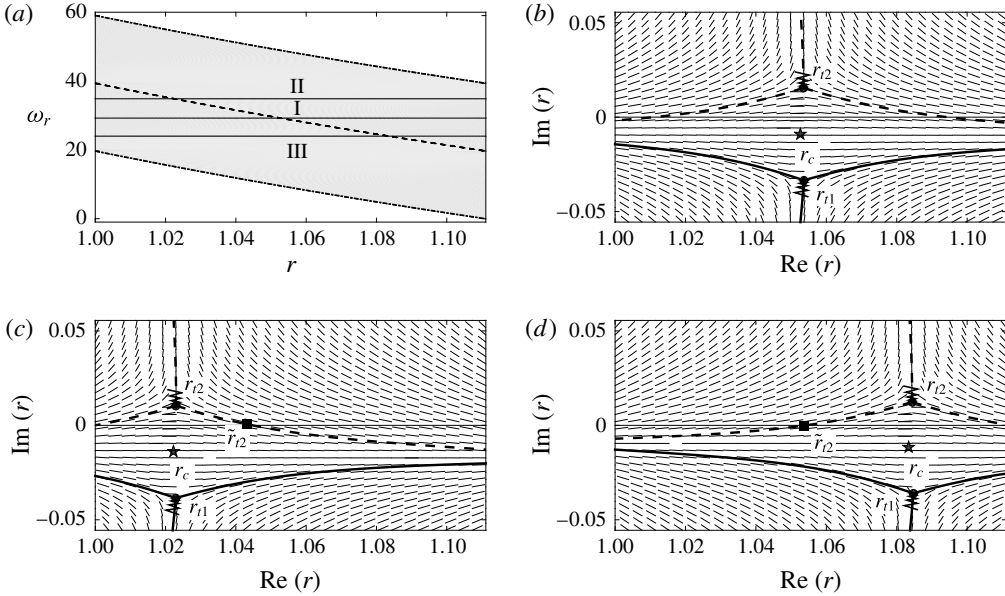


FIGURE 9. (a) Real part of epicyclic frequencies ω_{\pm} (thick dashed lines) and $\omega_{N\pm}$ (thick dash-dotted lines), and critical frequency ω_c (dashed line) for $m = 20$, $F = 1/20$, $\mu = 0.5$ and $\eta = 0.9$. The solid lines I, II and III correspond to the frequencies $\omega_r = 29.72$ (frequency of the SRI eigenmode shown in figure 8a), $\omega_r = 35.43$ (frequency of the CI eigenmode shown in figure 8b) and $\omega_r = 24.39$ (frequency of the CI eigenmode shown in figure 8c), respectively. Stokes line networks for (b) $\omega = 29.72 + 1.61i$, (c) $\omega = 35.43 + 2.75i$ and (d) $\omega = 24.39 + 1.94i$ correspond to the eigenmodes shown in figure 8. The representation is the same as in figure 4 and the parameters are the same as in (a).

4.2. Conditions of existence for the SRI

In the regime $0 \leq \mu \leq \eta^2$, the Rayleigh discriminant $\phi(r)$ is negative everywhere since the radius r_0 , where $\phi(r_0) = 0$, is larger than the radius of the outer cylinder r_o (i.e. $r_0 = \sqrt{(1-\mu)/(\eta^2-\mu)} > r_o$). Thus, $\text{Re}(\omega_+) = \text{Re}(\omega_-) = \text{Re}(\omega_c)$ as displayed in figure 9(a) for $m = 20$, $F = 1/20$, $\mu = 0.5$ and $\eta = 0.9$. The conditions for the existence of the SRI are the same as for $\mu < 0$, i.e. $\min(\omega_{N+}) > \max(\omega_{N-})$, $\max(\text{Re}(\omega_-)) > \max(\omega_{N-})$, $\min(\omega_{N+}) > \min(\text{Re}(\omega_+))$, $\max(\text{Re}(\omega_-)) > \max(\text{Re}(\omega_+))$, but they lead only to

$$\frac{1}{F} > \frac{m}{2} \left(\frac{1}{\mu} - 1 \right), \quad m > 0, \quad (4.1)$$

instead of (3.4). These conditions imply that the SRI can occur for any non-axisymmetric wavenumber provided that the stratification is sufficiently strong.

4.3. Complex WKBJ analysis

To understand the structure of the different modes in the framework of the WKBJ approach, the Stokes line networks for three representative eigenvalues are plotted in the complex plane in figure 9(b–d). Figure 9(b) corresponds to the mode I shown in figure 8(a), i.e. the first peak of SRI ($\omega = 29.72 + 1.61i$ at $k = 110$). The Stokes line network is similar to the one in figure 4(b) for the SRI for $\mu = -1$ except that the two

turning points are farther apart. A turning point has two Stokes lines crossing the real axis between the two cylinders $r_i < r < r_o$. There are therefore three distinct regions on the real axis in figure 9(b) like for the SRI for $\mu = -1$ (figures 4a,b). Figure 9(c) is an example of the Stokes line network of the mode II (figure 8b) which belongs to the first upper branch of CI ($\omega = 35.43 + 2.75i$ at $k = 400$). In this case, only one Stokes line crosses the real axis between the two cylinders and a second Stokes line is connected to the inner cylinder at $r = r_i$ like for $\mu = -1$ (figure 4c). Hence, there are two distinct regions as in figure 4(c). However, a difference is that the Stokes lines originate from the upper turning point r_{i2} instead of the lower turning point r_{i1} . Thus, the WKBJ dispersion relation for this case is simply (3.7) with r_{i1} replaced by r_{i2} :

$$\frac{i - \exp\left(-2ik \int_{r_i}^{r_{i2}} \sqrt{\beta} dt\right)}{1 - i \exp\left(-2ik \int_{r_i}^{r_{i2}} \sqrt{\beta} dt\right)} + \frac{1}{2} \exp\left(-2k \int_{r_{i2}}^{r_o} \sqrt{-\beta} dt\right) = 0. \quad (4.2)$$

However, this change has no effect and (4.2) leads at leading order in k to the same explicit dispersion relation as (3.10). This implies that the upper CI branches tend to $\omega \rightarrow m\Omega(r_i) + i\sqrt{-\phi(r_i)}$ as k goes to infinity. The asymptotic dispersion relations (4.2) (circles) and (3.10) (dashed line) are in good agreement with the numerical results as seen in figure 7. Surprisingly, the asymptotic dispersion relation (4.2) not only approximates very well the CI, but also the SRI. This good agreement for the SRI comes probably from the fact that the second Stokes line crosses the real axis close to $r = r_i$. Hence, the error made by assuming the WKBJ approximation (3.2) at $r = r_i$ is weak. For this reason, we have not performed a specific WKBJ analysis for the SRI in this case.

However, (4.2) is not able to describe the lower branches of the CI. In order to understand this, figure 9(d) shows the Stokes line network of the mode III (figure 8c) belonging to the first lower branch ($\omega = 24.39 + 1.94i$ at $k = 400$). The network is similar to the one for the first upper branch in figure 9(c) except that one Stokes line is connected to $r = r_o$ instead of $r = r_i$. Hence, the configuration is reversed compared to figure 9(c). The WKBJ approximation for $\tilde{r}_{i2} < r < r_o$ (where \tilde{r}_{i2} is the radius where the second Stokes line crosses the real axis) reads

$$u_r = \frac{Q^{1/2}}{r^{1/2}\beta^{1/4}} \left[D_+ \exp\left(ik \int_{r_{i2}}^r \sqrt{\beta(t)} dt\right) + D_- \exp\left(-ik \int_{r_{i2}}^r \sqrt{\beta(t)} dt\right) \right], \quad (4.3)$$

where D_{\pm} are constants. Using the same procedure as in §3.3, it can be shown that (4.3) matches the following WKBJ approximation for $r_i < r < \tilde{r}_{i2}$:

$$u_r = \frac{Q^{1/2}e^{-i\pi/4}}{r^{1/2}(-\beta)^{1/4}} \left[E_+ \exp\left(k \int_r^{r_{i2}} \sqrt{-\beta(t)} dt\right) + E_- \exp\left(-k \int_r^{r_{i2}} \sqrt{\beta(t)} dt\right) \right], \quad (4.4)$$

where $E_+ = D_+ + iD_-$ and $E_- = (iD_+ + D_-)/2$. Applying the boundary conditions at both cylinders, we obtain the asymptotic dispersion relation

$$\frac{2i + \exp\left(-2k \int_{r_i}^{r_{i2}} \sqrt{\beta} dt\right)}{2 + i \exp\left(-2k \int_{r_i}^{r_{i2}} \sqrt{\beta} dt\right)} - \exp\left(-2ik \int_{r_{i2}}^{r_o} \sqrt{-\beta} dt\right) = 0. \quad (4.5)$$

This relation can be also simplified further at leading order in k to

$$k \int_{r_{i2}}^{r_o} \sqrt{\beta} dt = \left(n_1 - \frac{1}{4}\right) \pi, \quad (4.6)$$

where n_1 is a positive integer. This implies that $\text{Im}(\int_{r_{i2}}^{r_o} \sqrt{\beta} dt) = \text{Re}(\int_{r_{i2}}^{r_o} \sqrt{-\beta} dt) = 0$ so that r_{i2} and r_o should be connected by a Stokes line as observed in figure 9(d). Since r_{i2} should be close to r_o as $k \rightarrow \infty$, we can obtain an explicit dispersion relation

$$\omega = m\Omega + i\sqrt{-\phi} - \frac{i(1/F^2 - \phi)}{2k^{2/3}\sqrt{-\phi}} \left[-\frac{3\pi}{2} \left(n_1 - \frac{1}{4}\right) \left(\frac{2im\sqrt{-\phi}\Omega' + \phi'}{1/F^2 - \phi} \right) \right]^{2/3} + \dots \quad (4.7)$$

This new dispersion relation is similar to (3.10) except that all the variables are now evaluated at $r = r_o$ instead of $r = r_i$. This implies that the eigenfrequency of the lower branches tends to $\omega \rightarrow m\Omega(r_o) + i\sqrt{-\phi(r_o)}$ as $k \rightarrow \infty$ instead of $\omega \rightarrow m\Omega(r_i) + i\sqrt{-\phi(r_i)}$ as $k \rightarrow \infty$ for the upper branches. Since $\phi(r)$ increases with r , $\sqrt{-\phi(r_i)}$ is larger than $\sqrt{-\phi(r_o)}$ explaining why the upper branches asymptote to a larger growth rate than the lower branches. As seen in figure 7, the asymptotic dispersion relations (4.5) (triangles) and (4.7) (dash-dotted lines) are in good agreement with the numerical results. It is worth mentioning that (4.5) and (4.7) should be also valid for $F \rightarrow \infty$. Hence, two types of centrifugal modes should also exist in homogeneous fluids for $0 \leq \mu \leq \eta^2$. The mode localized near the outer cylinder has been also reported recently by Leclercq *et al.* (2016). We recall that only the mode localized near the inner cylinder can exist for $\mu < 0$ because the Rayleigh discriminant is positive near the outer cylinder.

4.4. Effects of the Reynolds and Froude numbers

The CI and SRI are also in competition in the regime $0 \leq \mu \leq \eta^2$ and the most dangerous instability will depend on the Reynolds and Froude numbers. Figure 10(a) shows growth rate as a function of the axial wavenumber k for $m = 20$, $F = 1/20$, $\mu = 0.5$, $\eta = 0.9$, $Sc = 1$ and for three Reynolds numbers. We clearly see that the growth rate decreases as the Reynolds number decreases. The first growth rate peak for each Reynolds number corresponds to the SRI while next peaks correspond to the CI. For these Reynolds numbers, the CI is less unstable than the SRI and is suppressed before the SRI as the Reynolds number decreases.

Figure 10(b) shows neutral stability curves for various azimuthal wavenumbers for $\mu = 0.5$, $\eta = 0.9$ and $Sc = 1$. The critical Reynolds number Re_o for a given azimuthal wavenumber increases with $1/F$ for weak stratification like for $\mu = -1$ (figure 6). For strong stratification, a sudden decrease followed by a re-increase of the critical Reynolds number is also observed for $m \geq 15$. This abrupt transition occurs when the SRI starts to exist, i.e. when $1/F > m/2$ as predicted by (4.1) for $\mu = 0.5$. The dominant instability on the overall neutral stability curve is the centrifugal instability for $1/F < 25$, either axisymmetric for $1/F \lesssim 7$, or non-axisymmetric for $7 \lesssim 1/F < 25$. For stronger stratification $1/F > 25$, the SRI becomes the dominant instability.

5. Transient growth of the stratified Taylor-Couette flow for $\mu = -1$

5.1. Optimal energy growth

We now investigate the transient growth of the perturbations in the linearly stable regime for exact counter-rotation $\mu = -1$, i.e. the regime below the overall neutral

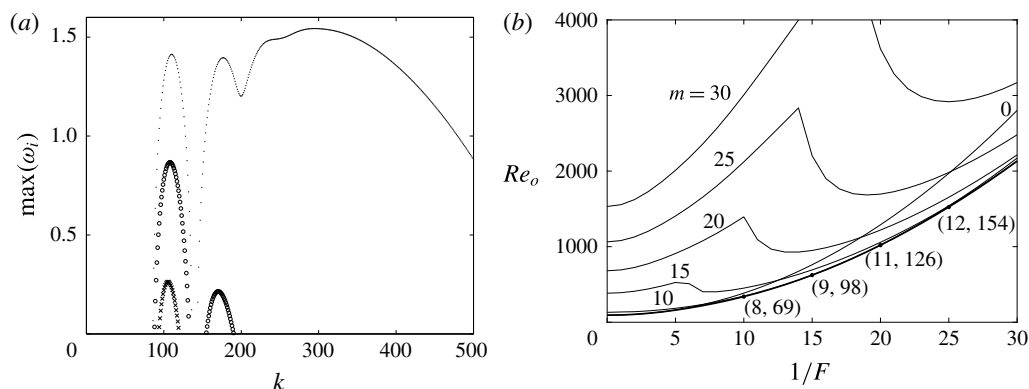


FIGURE 10. (a) Maximum growth rate $\max(\omega_i)$ as a function of axial wavenumber k for $m=20$, $F=1/20$, $\mu=0.5$, $\eta=0.9$, $Sc=1$ and for various Reynolds numbers: $Re_o=15000$ (dot), $Re_o=3000$ (empty circle) and $Re_o=1500$ (cross). (b) Neutral stability curves in the parameter space $(1/F, Re_o)$ for various azimuthal wavenumbers for $\mu=0.5$, $\eta=0.9$ and $Sc=1$. The thick solid line represents the neutral stability curve for all azimuthal wavenumbers. The numbers (m_{max}, k_{max}) , indicated at few selected points along this neutral curve, give the dominant azimuthal and axial wavenumbers m_{max}, k_{max} .

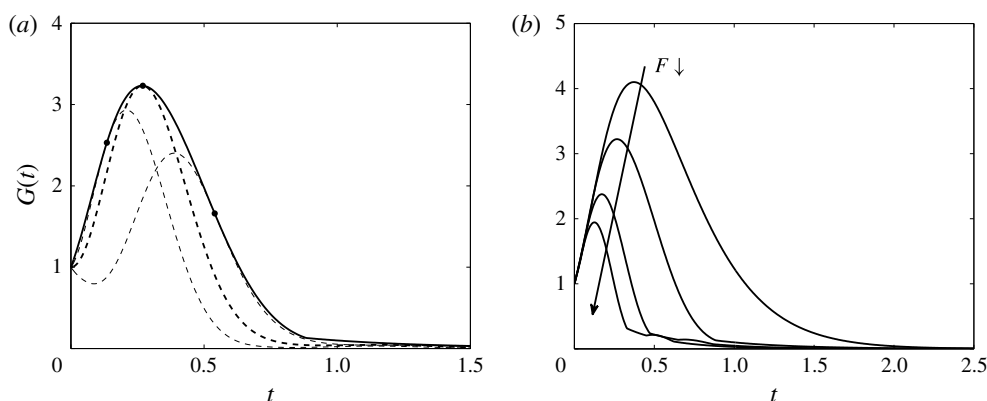


FIGURE 11. (a) Optimal energy growth $G(t)$ (thick solid) and energy growth (dashed) of selected initial perturbations which lead to optimal transient growths at the target times (dots) $t = t_o/2$, $t = t_o$ and $t = 2t_o$ for $m=0$, $k=34$, $Re_o=123.5$, $1/F=10$, $\mu=-1$, $\eta=0.9$ and $Sc=1$. The thick dashed line corresponds to the energy growth of the optimal perturbation. (b) $G(t)$ as a function of time t for $(1/F, k) = (0, 30)$, $(10, 34)$, $(20, 39)$ and $(30, 42)$ (top to bottom) for $Re=123.5$, $m=0$, $\mu=-1$, $\eta=0.9$ and $Sc=1$.

stability curve in figure 6. We first consider the transient growth of axisymmetric perturbations, $m=0$. Figure 11(a) shows the optimal energy growth $G(t)$ (solid line) for $k=34$, $Re_o=123.5$ and $1/F=10$. Figure 11(a) displays also the energy growths of different perturbations (dashed lines) which lead to the optimal energy growth at the target times $t = t_o/2$, $t = t_o$ and $t = 2t_o$, where t_o is the time at which the maximum energy growth G_{max} is attained: $G(t_o) = G_{max}$. The axial wavenumber $k=34$ corresponds to the maximum of G_{max} among all axial wavenumbers. We see that the transient growth behaviours of the perturbations differ for different target times. However, we shall only consider herein the optimal perturbation which

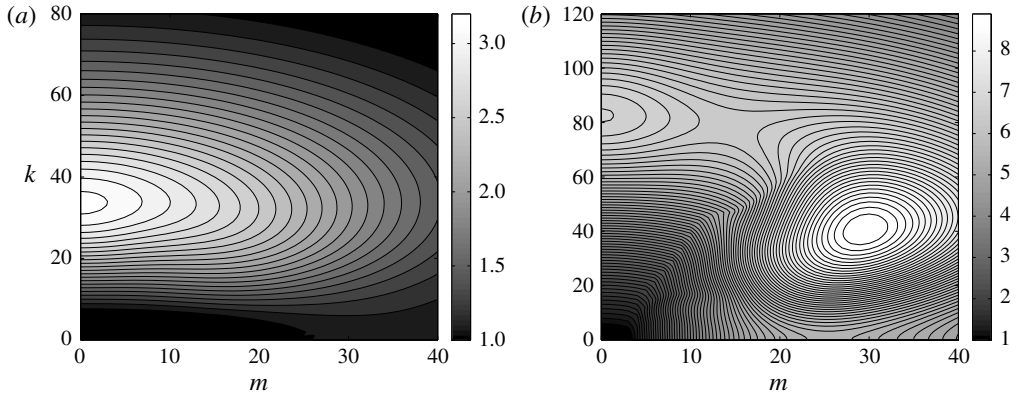


FIGURE 12. Contour plots of G_{\max} as a function of the azimuthal and axial wavenumbers (m, k) for $\mu = -1$, $\eta = 0.9$, $Sc = 1$ and for (a) $Re_o = 123.5$, $F = 1/10$ and (b) $Re_o = 740.7$, $F = 1/30$. The contour interval is 0.1.

achieves the maximum energy growth G_{\max} . Figure 11(b) shows the optimal energy growth $G(t)$ as a function of time t for different stratifications $1/F = (0, 10, 20, 30)$ for the same Reynolds number $Re_o = 123.5$. The corresponding axial wavenumbers $k = (30, 34, 39, 42)$ are those which give the optimal energy growth G_{\max} among all axial wavenumbers. We clearly see that the optimal energy growth G_{\max} and the optimal time t_o where $G(t_o) = G_{\max}$ decrease as the stratification increases. The optimal axial wavenumber increases as the stratification increases as observed by Boubnov *et al.* (1995) and Caton *et al.* (2000) for the linear dominant instability for $\mu = 0$ and by Yim & Billant (2016) for the centrifugal instability of vortices in strongly stratified fluid.

Figure 12 shows contour plots of the maximum optimal energy growth G_{\max} as a function of the azimuthal and axial wavenumbers (m, k) for (a) $Re_o = 123.5$, $F = 1/10$ and (b) $Re_o = 740.7$, $F = 1/30$. As already mentioned, the maximum value of $G_{\max} = 3.23$ for the first case is reached at $k = 34$ and $m = 0$ while, for the second case, we have $G_{\max} = 8.99$ at $k = 42$ and $m = 30$. Thus, non-axisymmetric perturbations lead to the maximal optimal energy growth in the second case in contrast to the first case.

Figure 13 summarizes in the parameter space $(1/F, Re_o)$ which type of perturbations, axisymmetric or non-axisymmetric, achieves the maximal optimal energy growth. The solid lines show the contours of $\max(G_{\max}) = \max_{m,k} G_{\max}$ over all axial wavenumbers and over all azimuthal wavenumbers while for the dashed contours, the azimuthal wavenumber is fixed to $m = 0$ (i.e. $\max_{m=0,k} G_{\max}$). We see that the axisymmetric perturbations achieve $\max(G_{\max})$ only when $1/F \lesssim 17$ or when the Reynolds number is low $Re_o \lesssim 200$ while non-axisymmetric perturbations lead to the maximal energy growth for high Reynolds numbers $Re_o \gtrsim 200$ and strong stratification $1/F \gtrsim 17$. The maximal energy growth decreases with F and increases with Re_o , attaining $O(50)$ values near the marginal stability. In the next section, we investigate the transient growth mechanisms of axisymmetric perturbations and non-axisymmetric perturbations.

5.2. Transient growth mechanisms

Figure 14 shows the temporal evolution of vorticity ω_θ , velocity u_θ and density ρ of the optimal perturbation in a vertical cross-section (r, z) for $k = 34$, $m = 0$,

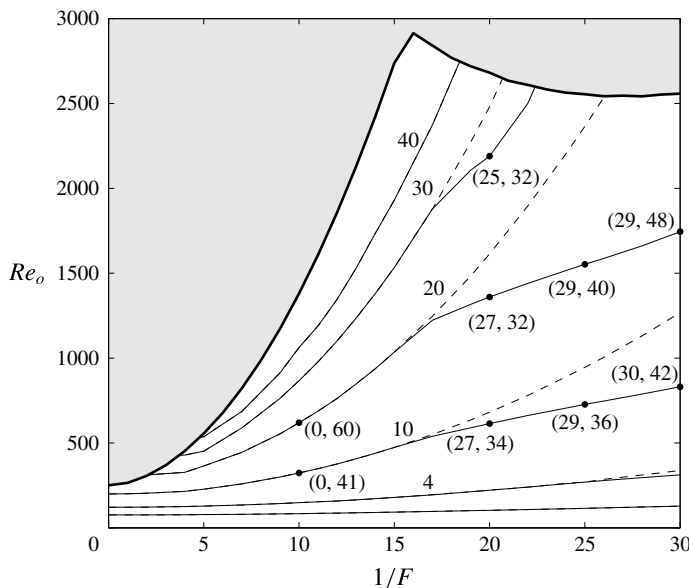


FIGURE 13. Contours of $\max(G_{\max})$ in the parameter space $(1/F, Re_o)$ for all axial wavenumbers and for all azimuthal wavenumbers (solid lines) and $m=0$ (dashed lines) for $\mu = -1$, $\eta = 0.9$ and $Sc = 1$. Numbers near the curves indicate the values of G_{\max} . The shaded region indicates the linearly unstable regime. The numbers (m, k) , indicated at few selected points along the contours, are the optimal azimuthal and axial wavenumbers which give $\max(G_{\max})$.

$Re_o = 123.5$ and $F = 1/10$. These wavenumbers correspond to the maximum of G_{\max} for $Re_o = 123.5$ and $F = 1/10$ (figure 12a). Since the perturbations ω_θ , u_θ and ρ have different orders of magnitude, they are each scaled by their own maximum values at $t = t_o$. The optimal initial perturbation leading to the maximum of G_{\max} consists of azimuthal vortices resembling Taylor vortices (figure 14a) and density perturbations (figure 14e) that are maximum or minimum near the inner and outer cylinders and that vanishes in between. As time evolves, azimuthal vortices and density perturbations generate azimuthal velocity streaks (figure 14b,c). After the optimization time t_o , the azimuthal velocity streaks and density perturbation decay (see figure 14d,h at $t = 2t_o$). This evolution is very similar to the lift-up effect observed for the Taylor–Couette flow in homogeneous fluids (Hristova *et al.* 2002). However, the strong density perturbations present in the optimal initial condition mean that the lift up involves here internal waves as shown by Bakas & Farrell (2009a,b) and Arratia (2011) for horizontal parallel shear layers in stratified fluids. The density perturbations associated with the internal waves initially produce vertical motions via the restoring baroclinic torque so as to enhance the azimuthal vortices that generate azimuthal velocity through the lift-up mechanism. This will be further shown below.

Similarly, figure 15 shows the temporal evolution of ω_θ , u_θ and ρ of the optimal perturbation for the wavenumbers $m=30$ and $k=42$ achieving the maximum of G_{\max} for $Re_o = 740.7$ and $F = 1/30$ (figure 12b). Unlike the axisymmetric perturbation, the non-axisymmetric optimal perturbation consists initially in oblique streaks, i.e. in azimuthal velocity perturbations inclined in the vertical plane (figure 15a) while the

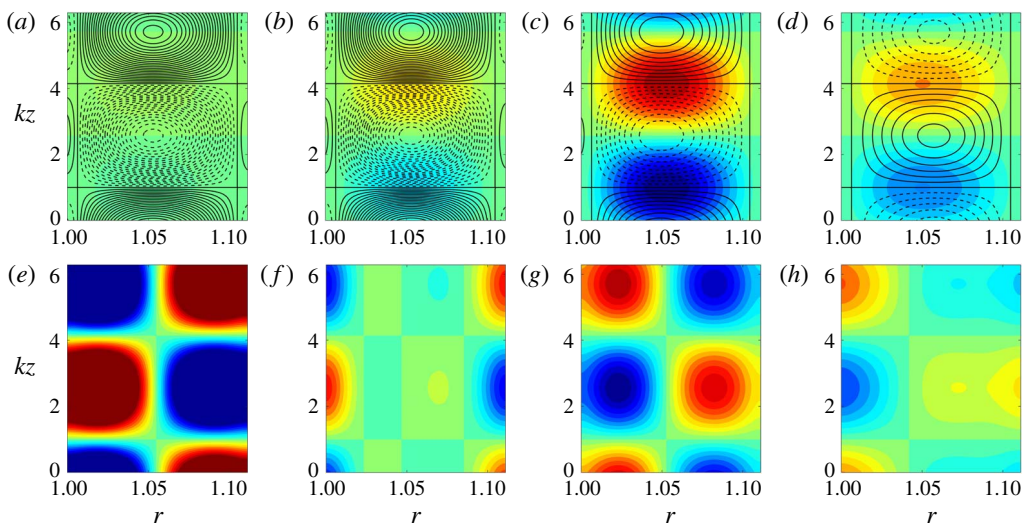


FIGURE 14. (Colour online) Temporal evolution of (a–d) velocity u_θ (colour) and vorticity ω_θ (black contours), and (e–h) density ρ of the optimal perturbation in a vertical cross-section (r, z) for $k = 34$, $m = 0$, $Re_o = 123.5$, $F = 1/10$, $\mu = -1$, $\eta = 0.9$ and $Sc = 1$: optimal perturbations at $t = 0$ (a,e), at $t = t_o/2$ (b,f), at $t = t_o = 0.27$ (c,g) and at $t = 2t_o$ (d,h). Black solid and dashed lines in (a–d) represent positive and negative values of ω_θ , respectively. Each quantity is scaled by its own maximum value at $t = t_o$. The contour interval for every quantity is 0.1.

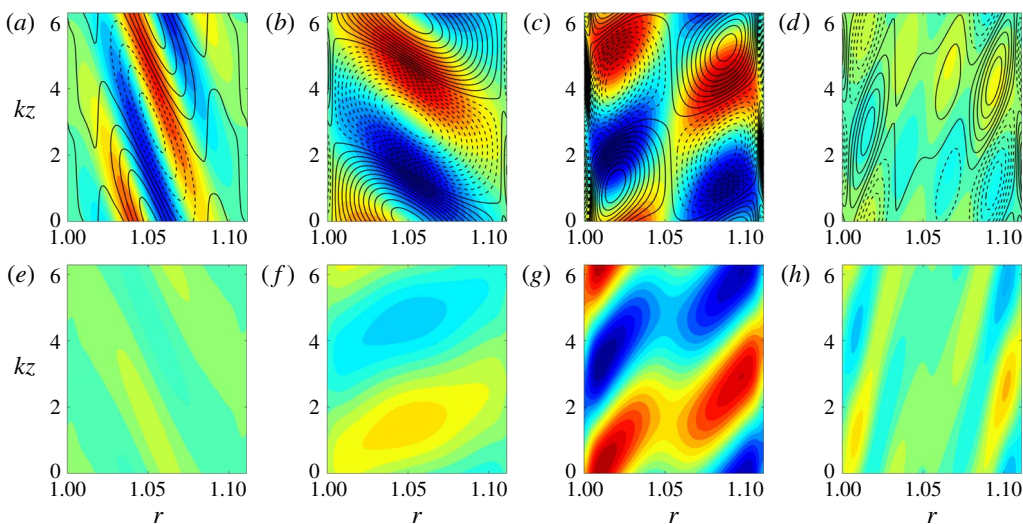


FIGURE 15. (Colour online) Same as figure 14 except for $k = 42$, $m = 30$, $Re_o = 740.7$ and $F = 1/30$.

density perturbations are weak at $t = 0$ (figure 15e). As time evolves, the azimuthal velocity perturbations rotate in anti-clockwise direction, i.e. the inclination angle of the streaks increases (figure 15b,c). At $t = t_o$, the azimuthal velocity perturbations

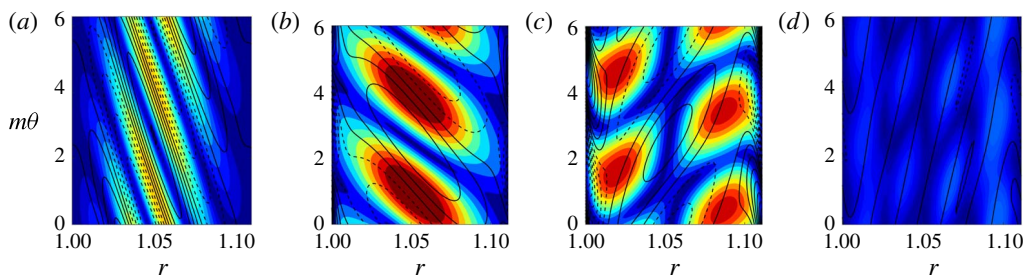


FIGURE 16. (Colour online) Temporal evolution of the horizontal velocity $u_h = \sqrt{u_r^2 + u_\theta^2}$ (colour) and vertical vorticity ω_z (black contours) of the optimal perturbation in the horizontal plane (r, θ) : optimal perturbations at $t=0$ (a), at $t=t_o/2$ (b), at $t=t_o=0.33$ (c) and $t=2t_o$ (d). The parameters are the same as in figure 15. Black solid and dashed lines represent positive and negative values of ω_z , respectively. The horizontal velocity u_h and vorticity ω_z are scaled by their own maximum values at $t=t_o$. The contour interval is 0.1.

(figure 15c) as well as the density perturbation (figure 15g) consists in two out-of-phase waves near each cylinder, somewhat like for the SRI (figure 2a).

Figure 16 further shows the evolution of horizontal velocity $u_h = \sqrt{u_r^2 + u_\theta^2}$ and vertical vorticity ω_z of the optimal perturbation in a horizontal cross-section (r, θ) . We clearly see that the vertical vorticity ω_z , which is initially strongly tilted against the direction of shear (the base angular velocity is negative at $r=r_i$ and positive at $r=r_o$), rotates so as to become aligned with the direction of shear at $t=t_o$. By this mechanism, the horizontal velocity u_h increase in amplitude. This is similar to the Orr mechanism (Orr 1907) by which perturbations initially tilted against the shear direction can grow transiently. However, the perturbations are actually three-dimensional as also observed in shear layers by Arratia (2011) and Kaminski *et al.* (2014). As shown by Bakas & Farrell (2009a,b) and Arratia (2011) for horizontal parallel shear layers, the effect of the Orr mechanism on such three-dimensional perturbations is to generate strong density perturbations (figure 15g) even if they are weak initially (figure 15e). Bakas & Farrell (2009a,b) have also shown that internal waves are generated near $t=t_o$ when $F_v = (k/m)2\eta F/(1-\eta)$ is of order unity. This parameter can be seen as a vertical Froude number based on the shear of the base flow and on the vertical length scale of the perturbations. Here, this vertical Froude number is approximately 0.8 but the emission of internal waves is difficult to ascertain from figures 15 and 16. For other Reynolds and Froude numbers, the wavenumbers (m_{max}, k_{max}) of the three-dimensional optimal perturbation (indicated at selected points in figure 13) are always such that F_v is of order unity.

Figure 17 shows the evolutions of the contribution of each velocity component to the kinetic energy and the potential energy:

$$E_r = \int_1^{1/\eta} \frac{\overline{\tilde{u}_r^2}}{2} r dr, \quad E_\theta = \int_1^{1/\eta} \frac{\overline{\tilde{u}_\theta^2}}{2} r dr, \quad E_z = \int_1^{1/\eta} \frac{\overline{\tilde{u}_z^2}}{2} r dr, \quad E_\rho = \int_1^{1/\eta} \frac{\overline{\tilde{\rho}^2}}{2F^2} r dr, \quad (5.1a-d)$$

where the overbar denotes the average in azimuthal and axial directions. The total energy $E = E_r + E_\theta + E_z + E_\rho$ is also plotted with dashed lines. In figure 17(a) where the parameters are the same as in figure 14, it shows that the potential energy is initially dominant while the kinetic energy of the azimuthal vortices (E_r and E_z) is

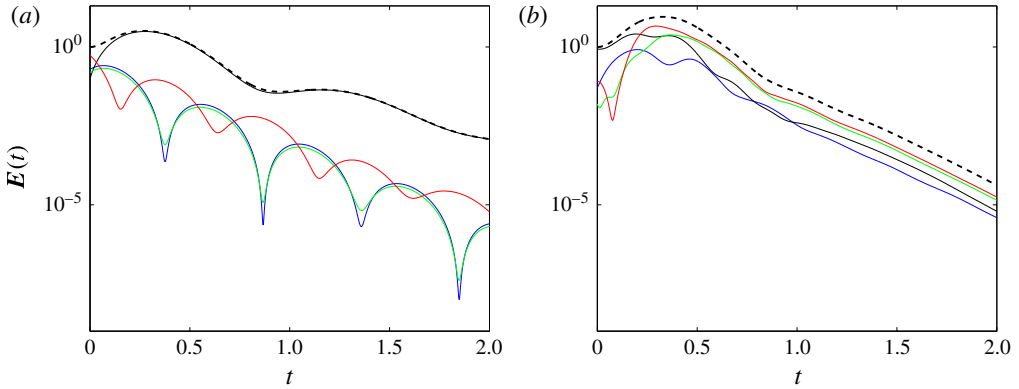


FIGURE 17. (Colour online) Temporal evolution of E_r (blue), E_θ (black), E_z (green), E_ρ (red) and total energy $E(t)$ (thick dashed lines) for $\mu = -1$, $\eta = 0.9$, $Sc = 1$ and for (a) $Re_o = 123.5$, $F = 1/10$, $m = 0$, $k = 34$ and (b) $Re_o = 740.7$, $F = 1/30$, $m = 30$, $k = 42$.

smaller but also significant. As time evolves, the kinetic energy E_θ increases while E_r , E_z and E_ρ decrease. At $t = t_o = 0.27$, the total energy $E(t)$ is dominated by E_θ . Subsequently, E_r , E_z and E_ρ decay as for the lift up in homogeneous shear flows but they exhibit oscillations. Moreover, the oscillations of E_ρ are out of phase with those of E_r and E_z . We can further notice that the period of oscillation of E_θ is twice the period of the other components. The period of oscillations of E_ρ , E_r and E_z is $T \simeq 0.49$ in figure 17(a). Other Froude numbers have also been studied and interestingly, the period varies like $T \simeq 4.9F$. This implies that the corresponding dimensional frequency is proportional to the Brunt–Väisälä frequency. It can be further shown that this period agrees fairly well with the non-dimensional dispersion relation of internal waves $\omega^2 = \cos^2 \theta / F^2$, where θ is the angle of the wavevector with the horizontal. From figure 14(a–d), we can estimate the non-dimensional radial wavenumber as $k_r = \pi r_i / (r_o - r_i) = \pi \eta / (1 - \eta) \approx 28$. If the cylindrical geometry is neglected, we have $\cos \theta = \sqrt{k_r^2 / (k^2 + k_r^2)} \approx 0.6$ since the vertical wavenumber is $k = (34, 39, 42)$ for $F = (1/10, 1/20, 1/30)$. The frequency is therefore $\omega \approx 0.6/F$ giving a period $T \approx 10F$ corresponding to a period $T/2 \approx 5F$ for the energy since it is a square quantity. This clearly shows that the lift-up mechanism in the stratified Taylor–Couette flow involves internal waves like for horizontal shear layer in stratified fluids (Bakas & Farrell 2009a,b; Arratia 2011). The period of oscillation of E_θ is T , instead of $T/2$ as for the other energy components, because the radial velocity that is induced by the internal waves is of the same sign as the radial velocity of the initial azimuthal vortices only every period T .

In contrast, the initial energy of the optimal perturbation in figure 17(b) which corresponds to the same parameters as figures 15 and 16 is dominated by E_θ as already seen in figure 15(a) by the inclined coloured contours. Initially, the kinetic energies E_r , E_θ , E_z increase while the potential energy E_ρ decreases. Later on, the potential energy increases dramatically and becomes dominant at $t = t_o = 0.33$. Hence, while the two-dimensional Orr mechanism would generate transient growth of only E_r and E_θ , the effect of the Orr mechanism on three-dimensional perturbations is to induce significant growth of both the potential and kinetic energies. Since the perturbation is three-dimensional, the increase of the horizontal velocity \tilde{u}_r and \tilde{u}_θ by the Orr mechanism is indeed associated with variations of the vertical pressure

gradient which in turn generates density perturbation through the hydrostatic balance. After $t = t_o$, the energy components E_ρ and E_z are significantly larger than the horizontal kinetic energy components E_r , E_θ . They decay monotonically without significant oscillations (figure 17*b*) as one would expect if large internal waves were excited like for unbounded shear flows (Bakas & Farrell 2009*a,b*; Arratia 2011). We have checked that this absence of oscillations is not due to the spatial integration performed in (5.1*a–d*). The vertical velocity and density perturbations take the form of two boundary waves near the inner and outer cylinders with zero azimuthal phase velocity at $r = r_i$ and $r = r_o$, respectively (see figure 15(*d,h*) at $t = 2t_o$).

The Orr mechanism can be understood from the evolution equation of the total energy E :

$$\frac{\partial E}{\partial t} = \int_1^{1/\eta} (-r\Omega' \tilde{u}_r \tilde{u}_\theta - \epsilon_K - \epsilon_P) r dr, \quad (5.2)$$

where $\epsilon_K = (\nabla \mathbf{u} : \nabla \mathbf{u})/Re$ and $\epsilon_P = (\nabla \rho : \nabla \rho)/(Re Sc F^2)$ are the dissipation of kinetic and potential energies. The first term on the right-hand side of (5.2) represents the transfer of kinetic energy from the base flow to the perturbation. This term is positive when $\tilde{u}_r \tilde{u}_\theta$ is negatively correlated with the angular velocity shear Ω' . It is the origin of the Orr mechanism.

In summary, the kinetic energy of axisymmetric perturbations can grow transiently through the lift-up effect which is coupled to internal waves in stratified fluids, while both the kinetic and potential energies of non-axisymmetric three-dimensional perturbations can grow transiently owing to the Orr mechanism.

6. Conclusions and discussions

In this paper, we have investigated the instabilities and transient growth of the Taylor–Couette flow in stratified fluids in the regime $\mu < \eta^2$ where the flow is inviscidly centrifugally unstable according to the Rayleigh criterion. Two different values have been studied: exact counter-rotation $\mu = -1$ and co-rotation $\mu = 0.5$ for the gap ratio $\eta = 0.9$. In the inviscid and non-diffusive limits, two types of instability, the centrifugal instability (CI) and the strato-rotational instability (SRI), exist. The CI is most unstable when the axial wavenumber k goes to infinity while the SRI occurs when two waves resonate at a finite k . The CI and SRI have also distinct eigenfunction structures. An asymptotic analysis has been performed for large k by means of the WKBJ approximation for both the CI and the SRI. The asymptotic dispersion relations are in very good agreement with the numerical results for both instabilities. When the viscous and diffusive effects are present, the numerical results show that both instabilities are stabilized. However, the CI is stabilized faster than the SRI as the buoyancy Reynolds number decreases when the stratification is sufficiently strong. Thus, the CI is the dominant instability on the neutral stability curve for weak and moderate stratification while the SRI is the dominant instability for strong stratification.

The transient growth of the stratified Taylor–Couette flow in the linearly stable regime for exact counter-rotation $\mu = -1$ has been also investigated for both axisymmetric and non-axisymmetric perturbations. For weak and moderate stratification or low Reynolds number, the maximum transient growth is attained by axisymmetric perturbations which initially consist in azimuthal vortices and a strong density perturbation associated with internal waves. They induce streaks in the azimuthal motion similarly to the lift-up effect in homogeneous fluids. On the other hand, for strong stratification and high Reynolds number, the maximum transient growth

is achieved by non-axisymmetric three-dimensional perturbations which are initially tilted against the shear direction. They lead to large amplifications of both kinetic energy and potential energy by the Orr mechanism. Boundary waves are generated by this mechanism but classical internal waves do not seem to be excited in contrast to unbounded horizontal shear layers in stratified fluids (Bakas & Farrell 2009a,b; Arratia 2011).

In summary, the stability analyses have revealed that the stratified Taylor–Couette flow in a Rayleigh-unstable regime is not always unstable primarily to the CI but another instability, the SRI, can be dominant. Secondly, we have shown that the dominant mechanism for transient growth is strongly dependent on the stratification.

In the future, it would be interesting to continue the study of the transient growth of the stratified Taylor–Couette flow, in particular to determine the effect of a non-unity Schmidt number. Indeed, Hua, Le Gentil & Orlandi (1997a) and Caton *et al.* (2000) have reported an axisymmetric oscillatory mode at onset of instability for $\mu = 0$ and $Sc \approx 700$ in the stratified Taylor–Couette flow. This is different from the steady axisymmetric mode or non-axisymmetric mode observed here for $Sc = 1$. Thus, it is likely that the transient growth mechanisms will also differ when Sc is different from unity. A study of the transient growth mechanisms in the regime $\mu > \eta^2$ where only the SRI can exist would also be of interest (Molemaker *et al.* 2001; Yavneh *et al.* 2001; Le Bars & Le Gal 2007; Park & Billant 2013b). Moreover, it could be interesting to study nonlinear transient growth as done for parallel shear flows (Monokrousos *et al.* 2011; Rabin, Caulfield & Kerswell 2012; Eaves & Caulfield 2015).

Acknowledgement

The first and third authors were supported by Korea Meteorological Administration Research and Development Program under grant KMIPA 2015-5190. We thank the reviewers for their constructive comments which have led to substantial improvements of the paper.

REFERENCES

- ABRAMOWITZ, M. & STEGUN, I. A. 1965 *Handbook of Mathematical Functions*. Dover.
- AGBESSI, Y., ALIBENYAHIA, B., NOUAR, C., HOF, L. C. B. & AVILA, M. 2015 Linear stability of Taylor–Couette flow of shear-thinning fluids: modal and non-modal approaches. *J. Fluid Mech.* **776**, 354–389.
- ANDERECK, C. D., LIU, S. S. & SWINNEY, H. L. 1986 Flow regimes in a circular Couette system with independently rotating cylinders. *J. Fluid Mech.* **164**, 155–183.
- ANTKOWIAK, A. 2005 Dynamique aux temps courts d’un tourbillon isolé. PhD thesis, Université Paul Sabatier de Toulouse.
- ARRATIA, C. 2011 Non-modal instability mechanisms in stratified and homogeneous shear flow. PhD thesis, Ecole Polytechnique.
- BAKAS, N. A. & FARRELL, B. F. 2009a Gravity waves in a horizontal shear flow. Part I: growth mechanisms in the absence of potential vorticity perturbations. *J. Phys. Oceanogr.* **39**, 481–496.
- BAKAS, N. A. & FARRELL, B. F. 2009b Gravity waves in a horizontal shear flow. Part II: interaction between gravity waves and potential vorticity perturbations. *J. Phys. Oceanogr.* **39**, 497–511.
- BAKAS, N. A., IOANNOU, P. J. & KEFALIAKOS, G. E. 2001 The emergence of coherent structures in stratified shear flow. *J. Atmos. Sci.* **58**, 2790–2806.
- BENDER, C. M. & ORSZAG, S. A. 1978 *Advanced Mathematical Methods for Scientists and Engineers*. McGraw-Hill.

- BILLANT, P. & CHOMAZ, J.-M. 2001 Self-similarity of strongly stratified inviscid flows. *Phys. Fluids* **13**, 1645–1651.
- BILLANT, P. & GALLAIRE, F. 2005 Generalized Rayleigh criterion for non-axisymmetric centrifugal instabilities. *J. Fluid Mech.* **542**, 365–379.
- BILLANT, P. & GALLAIRE, F. 2013 A unified criterion for the centrifugal instabilities of vortices and swirling jets. *J. Fluid Mech.* **734**, 5–35.
- BILLANT, P. & LE DIZÈS, S. 2009 Waves on a columnar vortex in a strongly stratified fluid. *Phys. Fluids* **21**, 106602.
- BOUBNOV, B. M., GLEDZER, E. B. & HOPFINGER, E. J. 1995 Stratified circular Couette flow: instability and flow regimes. *J. Fluid Mech.* **292**, 333–358.
- CATON, F., JANIAUD, B. & HOPFINGER, E. J. 2000 Stability and bifurcations in stratified Taylor–Couette flow. *J. Fluid Mech.* **419**, 93–124.
- CHEN, C., WAN, Z.-H. & ZHANG, W.-G. 2015 Transient growth in Taylor–Couette flow of a Bingham fluid. *Phys. Rev. E* **91**, 043202.
- COLES, D. 1965 Transition in circular Couette flow. *J. Fluid Mech.* **21**, 385–425.
- DUBRULLE, B., DAUCHOT, O., DAVIAUD, F., LONGARETTI, P.-Y., RICHARD, D. & ZAHN, J.-P. 2005a Stability and turbulent transport in Taylor–Couette flow from analysis of experimental data. *Phys. Fluids* **17**, 095103.
- DUBRULLE, B., MARIÉ, L., NORMAND, C., RICHARD, D., HERSANT, F. & ZAHN, J.-P. 2005b An hydrodynamic stability shear instability in stratified disks. *Astron. Astrophys.* **29**, 1–13.
- EAVES, T. S. & CAULFIELD, C. P. 2015 Disruption of SSP/VWI states by a stable stratification. *J. Fluid Mech.* **784**, 548–564.
- FARRELL, B. F. & IOANNOU, P. J. 1993 Transient development of perturbations in stratified shear flow. *J. Atmos. Sci.* **50**, 2201–2214.
- GROSSMANN, S., LOHSE, D. & SUN, C. 2016 High-Reynolds number Taylor–Couette turbulence. *Annu. Rev. Fluid Mech.* **48**, 53–80.
- HITCHMAN, H. M., LEOVY, C. B., GILLE, J. C. & BAILEY, P. K. 1987 Quasi-stationary zonally asymmetric circulations in the equatorial lower mesosphere. *J. Atmos. Sci.* **44**, 2219–2236.
- HRISTOVA, H., ROCH, S., SCHMID, P. J. & TUCKERMAN, S. L. 2002 Transient growth in Taylor–Couette flow. *Phys. Fluids* **14**, 3474–3484.
- HUA, B. L., LE GENTIL, S. & ORLANDI, P. 1997a First transitions in circular Couette flow with axial stratification. *Phys. Fluids* **9**, 365–375.
- HUA, B. L., MOORE, D. W. & LE GENTIL, S. 1997b Inertial nonlinear equilibration of equatorial flows. *J. Fluid Mech.* **331**, 345–371.
- KAMINSKI, A. K., CAULFIELD, C. P. & TAYLOR, J. R. 2014 Transient growth in strongly stratified shear layers. *J. Fluid Mech.* **758**, R4.
- LE BARS, M. & LE GAL, P. 2007 Experimental analysis of the stratorotational instability in a cylindrical Couette flow. *Phys. Rev. Lett.* **99**, 064502.
- LE DIZÈS, S. & BILLANT, P. 2009 Radiative instability in stratified vortices. *Phys. Fluids* **21**, 096602.
- LE DIZÈS, S. & LACAZE, L. 2005 An asymptotic description of vortex Kelvin modes. *J. Fluid Mech.* **542**, 69–96.
- LE DIZÈS, S. & RIEDINGER, X. 2010 The strato-rotational instability of Taylor–Couette and Keplerian flows. *J. Fluid Mech.* **660**, 147–161.
- LECLERQ, C., NGUYEN, F. & KERSWELL, R. R. 2016 Connections between centrifugal, stratorotational, and radiative instabilities in viscous Taylor–Couette flow. *Phys. Rev. E* **94**, 043103.
- MARETZKE, S., HOF, B. & AVILA, M. 2014 Transient growth in linearly stable Taylor–Couette flows. *J. Fluid Mech.* **742**, 254–290.
- MESEGUER, A. 2002 Energy transient growth in the Taylor–Couette problem. *Phys. Fluids* **14**, 1655–1660.
- MOLEMAKER, M. J., MCWILLIAMS, J. C. & YAVNEH, I. 2001 Instability and equilibration of centrifugally stable stratified Taylor–Couette flow. *Phys. Rev. Lett.* **86**, 5270–5273.

- MONOKROUSOS, A., BOTTARO, A., BRANDT, L., DI VITA, A. & HENNINGSON, D. S. 2011 Nonequilibrium thermodynamics and the optimal path to turbulence in shear flows. *Phys. Rev. Lett.* **106**, 134502.
- OLVER, F. W. J. 1974 *Asymptotics and Special Functions*. Academic.
- ORR, W. M. F. 1907 The stability or instability of the steady motions of a perfect liquid and of a viscous liquid. Part II: a viscous liquid. *Proc. R. Irish Acad. A* **27**, 69–138.
- PARK, J. 2012 Waves and instabilities on vortices in stratified and rotating fluids. PhD thesis, Ecole Polytechnique.
- PARK, J. & BILLANT, P. 2012 Radiative instability of an anticyclonic vortex in a stratified rotating fluid. *J. Fluid Mech.* **707**, 381–392.
- PARK, J. & BILLANT, P. 2013a Instabilities and waves on a columnar vortex in a strongly stratified and rotating fluid. *Phys. Fluids* **25**, 086601.
- PARK, J. & BILLANT, P. 2013b The stably stratified Taylor–Couette flow is always unstable except for solid-body rotation. *J. Fluid Mech.* **725**, 262–280.
- RABIN, S. M. E., CAULFIELD, C. P. & KERSWELL, R. R. 2012 Triggering turbulence efficiently in plane Couette flow. *J. Fluid Mech.* **712**, 244–272.
- RAYLEIGH, LORD 1917 On the dynamics of revolving fluids. *Phil. Trans. R. Soc. Lond. A* **93**, 148–154.
- SCHMID, P. J. & HENNINGSON, D. S. 2001 *Stability and Transition in Shear Flows*. Springer.
- SHALYBKOV, D. & RÜDIGER, G. 2005 Stability of density-stratified viscous Taylor–Couette flows. *Astron. Astrophys.* **438**, 411–417.
- SMYTH, W. D. & MCWILLIAMS, J. C. 1998 Instability of an axisymmetric vortex in a stably stratified, rotating environment. *Theor. Comput. Fluid Dyn.* **11**, 305–322.
- TAYLOR, G. I. 1923 Stability of a viscous liquid contained between two rotating cylinders. *Phil. Trans. R. Soc. Lond. A* **223**, 289–343.
- WITHJACK, E. M. & CHEN, C. F. 1974 An experimental study of Couette instability of stratified fluids. *J. Fluid Mech.* **66**, 725–737.
- WITHJACK, E. M. & CHEN, C. F. 1975 Stability analysis of rotational Couette flow of stratified fluids. *J. Fluid Mech.* **68**, 157–175.
- YAVNEH, I., MCWILLIAMS, J. C. & MOLEMAKER, M. J. 2001 Non-axisymmetric instability of centrifugally stable stratified Taylor–Couette flow. *J. Fluid Mech.* **448**, 1–21.
- YIM, E. & BILLANT, P. 2016 Analogies and differences between the stability of an isolated pancake vortex and a columnar vortex in stratified fluid. *J. Fluid Mech.* **796**, 732–766.